except for the resolution with L-**12**. As shown in these screening results, diacidic resolving agents L-**9** and L-**15** showed relatively higher resolution efficiency (E >60%) (entries 7 and 13). To our surprise, these resolving agents formed the acidic salt with a 1:1 molar ratio (diacidic resolving agent **9** or **15**/amine **2**), despite using an equimolar amount of diacidic resolving agents. Although this phenomenon of acidic salt formation has not yet been clarified at present, it is clear that the acidic salt is much more stable than the neutral salt (**9** or **15/2** = 1:2 molar ratio).

On the basis of these experimental results, it is concluded that enantiopure **2** could be resolved by using diacidic resolving agent L-**9** or L-**15** as a new resolving agent. However, the chiral purity of the salt with L-**9** (80% de) was relatively low compared with that with L-**15** (95% de), and therefore multiple salt recrystallization would not be avoided. From an industrial point of view, a lesser number of operation steps was desirable and so the resolution condition using L-**15** was further optimized as shown below.

2.2. Optimization of resolution conditions for racemic 2 with L-15

In order to fairly optimize resolution condition suited for practical operation on an industrial scale, we focused on (1) solute concentration, (2) molar ratio of resolving agent, and (3) further optimization based on the Pope and Peachey method.

2.2.1. Effect of solute concentration

In order to know stability of resolution reaction and to maximize productivity (product kg/batch), the effect of solute concentration was examined. Experimental results are summarized in Table 2.

Table 2
Effect of solute concentration in MeOH solvent

Entry	Substrate concentration % (w/w)	MeOH/**2** % (w/w)	Yield (%)	de (%)	E (%)
1	30	7.2	83	>99.5	83
2	40	4.3	87	99.3	86
3	50	2.9	86	98.8	85

As shown in Table 2, it was found that resolution efficiency (E) remained unchanged in a range of solute concentrations between 30% and 50% (w/w). This result suggests that the resolution system is extremely stable. Therefore, optimization of the resolution condition was performed in a range of solute concentrations between 40% and 50% (w/w).

2.2.2. Effect of molar ratio of resolving agent L-15

In order to find economic conditions without any deterioration of productivity, the effect of molar ratio of resolving agent L-**15** was examined. Experimental results are summarized in Table 3.

Table 3
Effect of molar ratio of resolving agent L-**15** in MeOH solvent

Entry	Molar ratio of **15** to racemic **2**[a]	Solute concentration % (w/w)	Salt composition ratio (R,R)-**2**/L-**15** (mol/mol)	Yield (%)	de (%)	E (%)
1	1.0	50	1/1	86	98.8	85
2	0.7	43	1/1	35	96.8	34
3	0.5	45	2/1	56	95.5	54

[a] Scale of racemic **2**: 30 mmol.

As shown in Table 3, it was found that a decrease in the molar ratio of L-**15** leads to a decrease in the resolution yield, whereas the chiral purity remained at a higher level (96–99%de). To our surprise, it was also found that molar ratio of (R,R)-**2**/L-**15** in the salt remained at 1:1, although L-**15** is less prevalent than **2** (entry 2, L-**15/2** = 0.7 (mol/mol)). On the other hand, when the molar ratio of L-**15** decreased to 0.5 (mol/mol), neutral conditions based on acid-base equilibrium, the molar ratio of (R,R)-**2**/L-**15** changed to neutral 2:1 as previously reported (entry 3).[1b] To our surprise, the chiral purity of the 2:1 salt remained higher than that observed in the 1:1 salt, although the resolution efficiency (E) was insufficient for industrialization.

From these test results, it was found that the best resolution condition was L-**15/2** = 1.0 (entry 1, E 88%). Moreover, the test results suggest that the composition molar ratio (1:1 or 2:1) of the salt does not affect the chiral purity, although yield was affected by the molar ratio of the resolving agent used. In other words, the molar ratio of the resolving agent is not a decisive factor for obtaining higher chiral purity. This result quickly prompted us to apply the Pope and Peachey method[10] using a supplementary acid while decreasing the molar ratio of L-**15** to racemic **2**.

2.2.3. Optimization of resolution condition based on the Pope and Peachey method

It is well known that the Pope and Peachey method can usually give better results in the salt yield by a salt-out effect with a more soluble salt formed between amine **2** and a supplementary acid (SA) such as HCl or AcOH. Since the present resolution system, composed of amine **2**, resolving agent L-**15**, and methanol, is extremely stable as described above, the resolution conditions were further optimized based on this method. Experimental results are summarized in Table 4.

Table 4
Optimization of resolution of racemic **2** with resolving agent L-**15** based on the Pope and Peachey method

Entry	Molar ratio of **15** to racemic **2**[a]	Supplementary acid		Yield (%)[b]	de (%)	E (%)
		Sort of acid	Molar ratio to **2**			
1	0.6	AcOH	0.4	52	99.4	52
2	0.6	HCl	0.4	92	99.5	92
3	0.5	HCl	0.5	84	98.8	83

[a] Solute concentration: 50% (w/w).
[b] Salt composition: 1:1 (mol/mol).

First, 0.4 M amount of HCl or AcOH was added into the resolution reaction in methanol (**2**/L-**15**/SA = 1.0/0.6/0.4 (mol/mol/mol); Table 4, entries 1 and 2). As a result, it was found that HCl gives a better result compared with that of using AcOH (E 92% and 51%, respectively). The result obtained by using HCl duly improved compared to that without SA (Table 4, entry 2 and Table 3, entry 1). On the other hand, when HCl content was increased to **2**/L-**15**/HCl = 1.0/0.5/0.5 (mol/mol/mol) the yield decreased, whereas the chiral purity remained in a high level (entry 3, 99.8%de, E 83%). These test results suggest that the Pope and Peachey method using HCl as a supplementary acid is extremely effective for obtaining better results compared with the usual resolution process with none of the supplementary acid (Tables 2 and 3).

3. Conclusion

A new resolution process for racemic *trans*-2-benzylaminocyclohexanol **2** was investigated. It was found that resolving agent L-**15** is quite effective as a resolving agent on the basis of stability and productivity of the resolution system for an industrial-scale production. The resolution conditions were optimized based on the Pope and Peachey method, and HCl was selected as a supplementary acid. The best result was obtained with racemic **2**/L-**15**/HCl = 1.0/0.6/0.4 (mol/mol/mol) (yield 92%, 99.5%de, E 92%).

4. Experimental

4.1. General

Racemic 2-benzylaminocyclohexanol **2** was prepared by the conventional method using the ring-opening reaction of cyclohexene oxide with benzylamine based on the proposed procedure.[1b] (*R*)-Mandelic acid **25** was purchased from Yamakawa Chemical Industry Co., Ltd (Tokyo), and was used without further purification. The other acidic resolving agents used in the resolution experiments were all made in Toray Fine Chemicals Co., Ltd (Tokyo)[11] and had high enantiomeric purities with over 99%ee. ^{1}H NMR spectra were recorded on a JEOL JNM-AL400 spectrometer (400 MHz for a proton), using CD_3OD and $CDCl_3$ as a solvent and tetramethylsilane as the internal reference. Elemental analysis was performed on Perkin Elmer CHNS/O 2400 II Analyzer. IR spectra were measured on a JASCO FT/IR-230 spectrometer in KBr pellets. Melting points were obtained on YAMATO apparatus MLDEL MP-21 and were uncorrected.

4.2. Determination of diastereomeric excess of 2 in the salt

The diastereomeric excess (%de) of the salt (=enantiomeric excess (%ee) of **2**) was determined by HPLC, CAPCELL PAK C18 SG120 (ID 4.6 mm × L 150 mm, Shiseido). The salt was treated with sodium hydroxide in water and the liberated amine **2** was extracted with $CHCl_3$. The separated organic layer was treated with GITC (2,3,4,6-tetra-*O*-acetyl-D-glucopyranosylisothiocyanate) prior to HPLC analysis to give an amine-GITC derivative. Analytical conditions were as follows: mobile phase 5 mM SDS (sodium dodecyl sulfate) aqueous solution/MeCN = 60/40 (v/v), detector UV (243 nm), column temperature 40 °C, elution rate 1.0 mL/min. Retention time: (*R*)-enantiomer 11.9 min, (*S*)-enantiomer 14.0 min.

4.3. Resolution of racemic 2 with L-15

A typical resolution procedure is as follows (Table 2, entry 1): To a 1 L flask were added 51.3 g of racemic **2** (250 mmol), 96.6 g of L-**15** (250 mmol), and 345 g of methanol followed by heating under stirring to obtain a clear solution at 65 °C. The solution was gradually cooled to 20 °C for about 3 h, and the precipitated diastereomeric salt was filtered off and washed with methanol (25 g) to yield wet salt crystals, followed by drying at 50 °C to afford (*R,R*)-**2**:L-**15** salt (63.7 g, 103.8 mmol, yield 83%, 99.8%de, *E* 83%).

Analytical data of the less-soluble diastereomeric salts obtained by the resolution are shown below. (*R,R*)-**2**:L-**15**: $[\alpha]_D^{20} = -110.3$ (*c* 1.0, MeOH); 99.8%de; mp 174–175 °C; IR (KBr) cm^{-1} 3440, 3166, 3068, 2946, 2926, 2862, 1725, 1612, 1541, 1404, 1338, 1266, 1240, 1178, 1111, 848, 754, 696; ^{1}H NMR (CD_3OD, 400 MHz): δ 8.00–8.02 (m, 4H), 7.27–7.46 (m, 9H), 5.88 (s, 2H), 4.23 (dd, J = 13.2, 10.8 Hz, 2H), 3.56 (br, 1H), 3.30 (s, 1H), 2.77 (d, J = 8.8 Hz, 1H), 2.40 (s, 6H), 2.10 (d, J = 10.8 Hz, 1H), 1.95 (s, 1H), 1.67–1.72 (m, 2H), 1.21–1.41 (m, 4H); Anal. Calcd for $C_{33}H_{37}NO_9$: C, 66.99; H, 6.30; N 2.37. Found: C, 66.90; H, 6.40; N, 2.35.

A typical resolution procedure based on the Pope and Peachey method is as follows (Table 4, entry 2): To a 100 mL flask were added 5.91 g of racemic **2** (29 mmol), 7.28 g of L-**15** (18 mmol), 1.25 g of 35% HCl aq (12 mmol), and 10.3 g of methanol followed by heating to obtain a clear solution at 65 °C. The solution was gradually cooled to 20 °C for about 3 h, and the precipitated diastereomeric salt was filtered off and washed with methanol (5 g) to yield wet salt crystals, which were dried at 50 °C to afford (*R,R*)-**2**:L-**15** salt (7.86 g, 13.3 mmol, yield 92%, 99.5%de, *E* 92%).

The less-soluble salt was treated with toluene and aqueous sodium hydroxide. The organic layer was separated and concentrated to give the crystalline product (*R,R*)-**2** with >99.5%ee. (*R,R*)-**2**: $[\alpha]_D^{20} = -91.2$ (*c* 1.0, MeOH); >99.5%ee; mp 90–91 °C (lit.[9] 92 °C); IR (KBr) cm^{-1} 3295, 3110, 3060, 3023, 2937, 2856, 2664, 2359, 2341, 1603, 1451, 1430, 1360, 1339, 1099, 1078, 972, 880, 844, 749, 699; ^{1}H NMR ($CDCl_3$, 400 MHz): δ 7.21–7.31 (m, 5H), 3.92 (d, J = 13.2 Hz, 1H), 3.76 (br, 1H), 3.65 (d, J = 13.0 Hz, 1H), 3.18 (dt, J = 14.9, 4.9 Hz, 1H), 2.25–2.31 (m, 1H), 2.11–2.15 (m, 1H), 1.97 (br, 1H), 1.68–1.71 (m, 2H), 1.17–1.29 (m, 4H), 0.94–1.03 (m, 1H).

References

1. (a) Jung, G.; Yee, J. G. K.; Chou, D. T. H.; Plouvier, B.M.C. WO. 2006, 138673.; (b) Plouvier, B. M. C.; Chou, D. T. H.; Jung, G. Choi, L. S. L.; Sheng, T.; Barrett, A. G. M.; Passafaro, M. S.; Kurz, M.; Moeckli, D.; Ulmann, P.; Hedinger, A. WO. 2006, 088525.
2. Koga, Y.; Kihara, Y.; Okada, M.; Inoue, Y.; Tochizawa, S.; Toga, K.; Tachibana, K.; Kimura, Y.; Nishi, T.; Hidaka, H. *Bioorg. Med. Chem. Lett.* **1998**, *8*, 1471.
3. Kobayashi, N.; Koji, T.; Fujita, T.; Nishimura, T.; Hosoda, A. WO. 2002, 02546.
4. Smith, R. A.; O'Connor, S. J.; Wirtz, S.-N.; Wong, W. C.; Choi, S.; Kluender, H. C. E.; Su, N.; Wang, G.; Achebe, F.; Ying, S. WO. 2003, 040107.
5. De (diastereomeric excess)% is based on the ee (enantiomeric excess)% of the amine liberated from the less-soluble diastereomeric salt. The yield is calculated based on half of the racemic amine. Resolution efficiency (*E*, %) = yield (%) × de (%)/100.
6. Kotake, M.; Oinuma, H.; Suda, S.; Yoneda, N.; Sato, K.; Mizuno, M.; Miyake, K. JP 09059252, 1997.
7. Zhang, G.; Liao, Y.; Wang, Z.; Nohira, H.; Hirose, T. *Tetrahedron: Asymmetry* **2003**, *14*, 3297.
8. Chatterjee, A.; Sasikumar, M.; Joshi, N. N. *Synth. Commun.* **2007**, *37*, 1727.
9. Shiffers, I.; Rantanen, T.; Schmidt, F.; Bergmans, W.; Lorenzo, Z.; Bolm, C. *J. Org. Chem.* **2006**, *71*, 2320.
10. Pope, W. J.; Peachey, S. J. *J. Chem. Soc.* **1899**, *75*, 1066; Our group had reported the resolution of the diamine compound, 3-aminopyrrolidine. See: Sakurai, R.; Yuzawa, A.; Sakai, K. *Tetrahedron: Asymmetry* **2008**, *19*, 1622.
11. (a) Fujino, T.; Sato, H. JP 09071571, 1997; (b) Nakai, S.; Sato, H. JP 09124595, 1997.

ASEDock-Docking Based on Alpha Spheres and Excluded Volumes

Junichi Goto and Ryoichi Kataoka

Computational Science Department, Science & Technology Systems Division, Ryoka Systems, Inc., 1-28-38 Shinkawa, Chuo-ku, Tokyo 104-0033, Japan

Hajime Muta and Noriaki Hirayama*

Basic Medical Science and Molecular Medicine, Tokai University School of Medicine, 143 Shimokasuya, Isehara, Kanagawa 259-1143, Japan

Received September 19, 2007

ASEDock is a novel docking program based on a shape similarity assessment between a concave portion (i.e., concavity) on a protein and the ligand. We have introduced two novel concepts into ASEDock. One is an ASE model, which is defined by the combination of alpha spheres generated at a concavity in a protein and the excluded volumes around the concavity. The other is an ASE score, which evaluates the shape similarity between the ligand and the ASE model. The ASE score selects and refines the initial pose by maximizing the overlap between the alpha spheres and the ligand, and minimizing the overlap between the excluded volume and the ligand. Because the ASE score makes good use of the Gaussian-type function for evaluating and optimizing the overlap between the ligand and the site model, it can pose a ligand onto the docking site relatively faster and more effectively than using potential energy functions. The posing stage through the use of the ASE score is followed by full atomistic energy minimization. Because the posing algorithm of ASEDock is free from any bias except for shape, it is a very robust docking method. A validation study using 59 high-quality X-ray structures of the complexes between drug-like molecules and the target proteins has demonstrated that ASEDock can faithfully reproduce experimentally determined docking modes of various druglike molecules in their target proteins. Almost 80% of the structures were reconstructed within the estimated experimental error. The success rate of ~98% was attained based on the docking criterion of the root-mean-square deviation (RMSD) of non-hydrogen atoms (≤2.0 Å). The markedly high success of ASEDock in redocking experiments clearly indicates that the most important factor governing the docking process is shape complementarity.

1. INTRODUCTION

Docking simulations between drug candidates and their target proteins are now one of the essential methodologies in many drug discovery projects. The docking simulation is practically an in silico counterpart of high-throughput screening (HTS). The chemical space that can be surveyed by docking simulations is significantly larger than that by HTS. Three-dimensional structures of many biologically important proteins are registered in the Protein Data Bank (PDB)[1] now, and the number of entries is expanding recently. The availability of reliable atomic coordinates of target proteins is also raising great expectations for the contribution of docking simulations to many drug discovery projects.

Many programs such as FLexX,[2] AutoDock,[3] GOLD,[4] Glide,[5] and Surflex[6] have been proposed, and some of them are actually contributing in discovering novel drug molecules. From this sense, the docking technology is edging close to practical use. Nevertheless, many essential problems regarding docking simulations are not solved yet and none of the currently available programs are perfect in predicting the correct binding modes. Therefore, the improvement of the performance of docking simulations is one of the priority subjects in drug discovery technologies.

* To whom correspondence should be addressed. Tel.: +81 463 93 1121. E-mail address: hirayama@is.icc.u-tokai.ac.jp.

We developed a docking program called Ph4Dock.[7] This program exploits the pharamacophoric features both in the ligand and the concave portions of the target protein. Although Ph4Dock gave quite a good performance in the redocking experiments of 43 quality X-ray structures of complexes between drug-like molecules and the target proteins, it failed to give reasonable answers to several structures. After applications of Ph4Dock to many problems, we have learned that Ph4Dock had two important drawbacks. First, in Ph4Dock, the pharmacophore model and the ligand are compared. However, the pharmacophore model cannot always accurately represent the landscape of the concavity, and the poor concordance between the pharmacophore model and the ligand was a reason for failure. Second, the accuracy of pharamacophore was not necessarily adequate in some cases, and manual intervention was required in the actual docking simulations. We have been generally satisfied with the docking performance by Ph4Dock, but, at the same time, the experiences on these problems have led us to think that we should put a high priority on the concordance of the shapes of concavity and the ligand. In this paper, we present a novel docking algorithm that is based on an accurate modeling of concavity shape and a function that evaluates the shape similarity between the model and the ligand. The novel algorithm has proven the markedly high performance

10.1021/ci700352q CCC: $40.75
Published on Web 02/16/2008

of redocking experiments for 59 high-quality X-ray structures of complexes between the drug-like molecules and the target proteins.

2. COMPUTATIONAL METHODS

MOE (Molecular Operating Environment)[8] was used as a developing platform of ASEDock. All of the algorithms of ASEDock were coded using MOE's powerful vector language SVL (Scientific Vector Language). Existing features implemented in MOE were fully applied to realize the functions of ASEDock.

ASEDock is mainly composed of the following five steps: (i) generation of conformations for a ligand, (ii) concavity search on the surface of a target protein, (iii) generation of an ASE model at a concavity, (iv) rigid body alignment of the ligand conformations to the ASE model, and (v) the energy minimization of the posed conformations of the ligand in the concavity.

2.1. Generation of Ligand Conformations. A stochastic conformation generation method is applied, as in Ph4Dock. The hydrogen atoms are added in accordance with the standard protonation states of acids and bases in biological molecules. The generalized Born solvation area model[9] is used in the conformation energy calculations. The MMFF94x force field was used.[10] The following two selection procedures are used to omit redundant conformations. First, the conformations are clustered if the root-mean square deviations (RMSDs) of the corresponding non-hydrogen atoms are <0.5 Å. Second, the most diverse conformations are selected from the clustered conformations as follows. The first conformer to be selected is the one with the minimum energy, the second one is the conformer with the largest RMSD from the first, the third one is selected to be most distant from the previous conformers, and so on.

2.2. Concavity Search and Generation of ASE Model. A concave portion designated as concavity at the surface of a receptor molecule where a ligand is supposed to bind is identified as a collection of spheres, using the modified Delaunay triangulation.[11] The sphere, which is called the "alpha sphere", is used to characterize the concavity as in Ph4Dock. Surrounding a concavity where a ligand is bound, there is a protein region where the ligand cannot access. The volume of such region, which is called the "excluded volume", can be evaluated using the non-hydrogen atoms of the protein within 5.5 Å from the alpha spheres. The excluded volume of each non-hydrogen atom is calculated using a sphere with the radius of 1.4 Å for the lone-pair active atoms (such as nitrogen and oxygen atoms) or 1.8 Å for the non lone-pair active atoms (such as carbon atoms). Hereafter, the sphere is designated as an "exclusion sphere". An ASE model is defined by the combination of alpha spheres and the excluded volumes around the concavity. The ASE model is used as a guide on which various ligand conformations treated as rigid bodies are posed.

2.3. ASE Score. Alpha spheres can be generated at the binding site. Maximizing the overlap of the ligand atoms with the alpha spheres and minimizing the overlap of the ligand atoms with the exclusion spheres would yield the optimal posing of the ligand on the ASE model. To evaluate the goodness of fit of a pose onto the ASE model, we have introduced a simple Gaussian overlap function:

$$\text{ASE Score} = -\sum_{i}^{a,e}\sum_{j}^{l} w_{i,j}\exp(-\alpha\, d_{i,j}^{2})$$

Here, d is the distance between a ligand atom and an alpha sphere or an exclusion sphere in the ASE model, and α is an adjustable parameter to attenuate the influence of a ligand atom when it is aligned to the alpha sphere or the exclusion sphere. The sums are taken over the alpha spheres (a), the exclusion spheres (e), and the ligand atoms (l). The parameter w is a weighting factor, being $+r_a r_l$ and $-r_e r_l$ for alpha and exclusion spheres, respectively; here, r_a, r_e, and r_l are the radii of the alpha spheres, the radii of the exclusion spheres, and van der Waals radii of the ligand atoms, respectively. The smaller the ASE score, the larger the overlap between the alpha spheres and the ligand atoms, and the smaller the overlap between the ligand atoms and the exclusion spheres. Because this function is a simple continuous one, it is easy to align a ligand to the ASE model and obtain reasonable posed structures in a short time by minimizing this function.

2.4. Posing and Rigid Body Alignment of Ligand to the ASE Model. The selected independent conformers are posed onto the ASE model. Three non-hydrogen atoms are sampled so that the area of the triangle becomes the largest. On the other hand, three alpha spheres are randomly selected to make multiple triangles. By overlapping these two types of triangles, conformers can be posed to the alpha spheres.

The initial poses of ligands are further optimized with the rigid-body alignment[12] by minimizing the ASE score with the Newton-Lapson method. This process converges relatively faster than that with the standard interaction function. The Gaussian function takes the finite value at the origin and has a gentle gradient, compared to the interaction functions. Therefore, even if the ligand overlaps with the protein, the value of the ASE score would not soar and can easily remove the overlap. The ASE score could be a robust scoring function to evaluate and steadily optimize the initial pose of the ligand at the concavity of the protein.

2.5. Energy Minimization. Posed conformations in a higher rank in the ASE score or the interaction energies are then subjected to be optimized by minimizing the following function:

$$U_{\text{total}} = U_{\text{ele}} + U_{\text{vdw}} + U_{\text{solv}} + U_{\text{ligand}}$$

Here, U_{ele}, U_{vdw}, and U_{solv} are Coulombic, van der Waals, and generalized Born/solvent accessible solvation interactions, respectively. U_{ligand} is the internal conformation energy of the ligand. The MMFF94x force field was used to calculate each energy term.

Because the potential energy calculation is the most time-consuming process in the docking calculations, we divided this process into two steps: rough minimization with a short cutoff distance from the alpha sites at first, and more-precise calculation with longer cutoff distance afterward. In the first step of rough minimization, a shorter cutoff distance of 4.5 Å and a convergence criterion of the root-mean square (RMS) gradient of 10 kcal/(mol Å) are used. The interaction energies are calculated with increasing cutoff distance to 8 Å and then the five structures with the minimum interaction energies or the maximum ASE scores are selected for the second optimization. In the second step of fine minimization, 5−10 structures are further refined by setting the cutoff

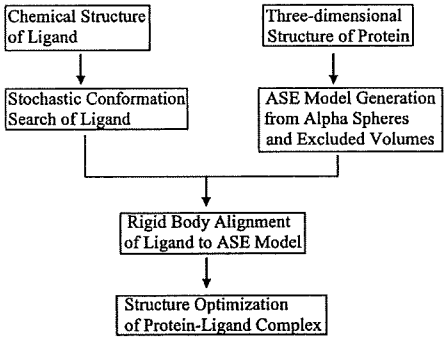

Figure 1. Flowchart of ASEDock.

distance and RMS gradient to be 8 Å and 0.1 kcal/(mol/Å), respectively.

ASEDock is mainly composed of six steps, as schematically shown in Figure 1.

2.6. Test Dataset. The best way to evaluate the potential of docking algorithms is reconstruction of the X-ray structures between proteins and ligands. If the structure of a ligand docked in the protein concords well with that in the crystal structure, we can judge that the docking algorithm may work well in a virtual screening. The precision of the atomic coordinates, as determined by X-ray analysis, is crucial for this evaluation. Therefore, we selected the best quality structures from PDB. The following five criteria are used to select the quality structure. First, the diffraction resolution and R_{free} are less than or equal to 2.5 Å and 0.24, respectively. These values guarantee that the X-ray analysis was undertaken well. Second, the occupancy factors of all non-hydrogen atoms in the structure are 1.0. This means that the protein structure is reasonably rigid and the docking calculations without including the effect of induced fit should be valid. Third, the ligand bound in the protein is drug-like. The drug-likeness of the ligand is judged by the criteria reported previously.[13] Fourth, the maximum temperature factors of non-hydrogen atoms in the ligand is $\leq$20 Å^2. This condition guarantees that the ligand molecule is tightly bound at the concavity. Fifth, covalently bound ligands and ligands that contain metal atoms were excluded from the scope of the target. Only 59 independent structures that fulfill the aforementioned criteria were screened from all PDB entries downloaded on June 12, 2007. The PDB codes of the structures, together with other information, are given in Table 1. The chemical names of the ligands together with a few physicochemical properties are given in Table 2. The ligands are sufficiently diverse. Therefore, these structures are suitable for redocking experiments.

In 1J4I and 1OIO, small molecules are not bound to the single protein; instead, they are entrapped between multiple proteins in the crystal structures, as shown in Figure 2. Since the small molecules contact with the multiple proteins in the crystals, three and two proteins surrounding the small molecules were considered for 1J4I and 1OIO, respectively, in regard to calculating the concavities.

2.7. Dielectric Constants. The nonbonded interatomic potential functions have crucial roles in molecular simulations. Especially in the docking simulations between a small molecule and a protein, the disposition and the structure of a small molecule can be highly affected by the nonbonded interactions with protein atoms. Therefore, the evaluation of the relevant interatomic interactions is critical in the docking simulations. A balance between electrostatic and van der Waals interactions is a key factor that affects the energy minimization process.

We have studied the effect of dielectric constant (ϵ) on the docking results of 59 complex structures in the test dataset. We especially paid attention to the effect of ϵ on hydrogen bond distances and the RMSDs of non-hydrogen

Table 1. Docking Results Obtained by ASEDock for 59 Protein−Ligand Complexes

PDB code	resolution (Å)	R_{free}	DPI (Å)	$2\sqrt{2}\sigma$ (Å)[a]	RMSD (Å)	lowest U_{total} (kcal/mol)
1azl	1.80	0.232	0.245	0.692	0.864	17.3
1c83	1.80	0.231	0.177	0.501	0.506	0.3
1c88	1.80	0.228	0.174	0.491	0.447	−0.6
1cbk	2.02	0.213	0.252	0.712	0.119	12.1
1cbs	1.80	0.237	0.218	0.615	0.462	8.9
1dbt	2.40	0.228	0.410	1.160	0.200	−10.8
1efi	1.60	0.231	0.215	0.609	0.407	49.0
1efv	2.10	0.222	0.343	0.972	0.159	−15.5
1eiz	1.70	0.237	0.202	0.573	0.543	18.5
1ekx	1.95	0.214	0.219	0.620	0.197	−77.7
1f5v	1.70	0.206	0.195	0.552	0.295	8.8
1f8y	2.40	0.218	0.365	1.033	0.280	15.9
1ftx	2.20	0.211	0.342	0.969	0.299	−31.6
1g2o	1.75	0.212	0.184	0.519	0.240	4.6
1gvo	1.38	0.200	0.110	0.311	0.432	21.8
1hjz	1.70	0.227	0.187	0.529	0.251	−2.6
1iei	2.50	0.199	0.492	1.391	0.341	28.0
1j4i	1.80	0.209	0.215	0.608	0.943	41.9
1ja9	1.50	0.221	0.121	0.342	0.116	12.1
1jak	1.75	0.192	0.125	0.353	0.960	−2.4
1kew	1.80	0.221	0.148	0.417	0.278	−60.7
1kkp	1.93	0.206	0.238	0.673	0.345	−8.2
1kll	1.93	0.197	0.226	0.638	0.275	−12.2
1kpg	2.00	0.233	0.315	0.890	0.554	22.5
1kt7	1.27	0.195	0.088	0.248	0.163	8.8
1l4g	2.10	0.226	0.345	0.976	0.249	7.8
1l5k	2.00	0.216	0.262	0.740	0.402	−5.1
1l5l	2.00	0.197	0.244	0.690	0.427	−9.8
1l5m	2.00	0.218	0.275	0.779	0.454	−11.2
1lc8	1.80	0.229	0.199	0.564	0.235	−55.8
1li4	2.01	0.236	0.265	0.749	0.200	3.3
1lii	1.73	0.225	0.188	0.530	0.591	27.7
1m2g	1.70	0.220	0.190	0.538	0.950	4.1
1mm7	1.65	0.237	0.180	0.509	0.354	−16.7
1mqj	1.65	0.229	0.160	0.453	0.166	−17.9
1mvc	1.90	0.228	0.070	0.199	0.370	52.7
1n1t	1.60	0.197	0.137	0.388	0.643	9.6
1n3i	1.90	0.213	0.226	0.638	0.229	0.1
1nvr	1.80	0.226	0.193	0.545	0.223	77.4
1oh0	1.10	0.220	0.058	0.165	0.557	40.1
1oio	1.70	0.238	0.123	0.349	0.366	9.8
1owe	1.60	0.236	0.205	0.579	0.427	29.1
1p4j	2.00	0.198	0.231	0.654	0.221	21.0
1pfy	1.93	0.224	0.255	0.721	0.504	21.9
1pg4	1.75	0.211	0.200	0.565	0.291	1.0
1r0p	1.80	0.197	0.190	0.539	0.223	62.8
1sg0	1.50	0.234	0.141	0.398	0.580	19.4
1t40	1.80	0.193	0.190	0.536	0.278	16.8
1tkg	1.50	0.219	0.136	0.384	4.019	19.6
1uf5	1.60	0.198	0.142	0.403	0.222	−22.3
1urg	1.80	0.217	0.202	0.571	0.554	41.8
1v7c	2.00	0.230	0.262	0.740	0.245	−47.1
1wap	1.80	0.225	0.215	0.608	0.166	−6.0
1wu6	1.45	0.180	0.099	0.280	0.178	37.1
1xoz	1.37	0.193	0.101	0.285	0.214	62.7
1yki	1.70	0.167	0.144	0.406	0.245	3.3
2ay3	2.40	0.221	0.506	1.432	0.371	17.7
2prj	2.30	0.237	0.437	1.237	0.253	9.4
2skc	2.40	0.217	0.433	1.225	0.242	10.1

[a] $\sigma = \sigma(r,B_{avg})$.

Table 2. Chemical Names and Some Physicochemical Properties of the Ligands

PDB code	ligand name	MW[a]	SlogP[b]	TPSA[c]	Nrot[d]
1azl	alrestatin	254.2	0.19	77.5	2
1c83	6-(oxalyl-amino)-1H-indole-5-carboxylic acid	246.2	−1.78	125.2	3
1c88	2-(oxalyl-amino)-4,5,6,7-tetrahydro-thieno [2,3-c]pyridine-3-carboxylic acid	269.3	−3.31	126.0	3
1cbk	7,8-dihydro-7,7-dimethyl-6-hydroxypterin	209.2	−1.90	108.6	0
1cbs	retinoic acid	299.4	4.27	40.1	5
1dbt	uridine-5′-monophosphate	322.2	−4.73	159.5	4
1efi	4′-aminophenyl-alpha-D-galactopyranoside	271.3	−1.55	125.4	3
1efv	adenosine monophosphate	346.2	−3.47	182.9	4
1eiz	*S*-adenosylmethionine	399.5	−3.88	187.1	7
1ekx	*N*-(phosphonacetyl)-L-aspartic acid	251.1	−6.80	160.6	6
1f5v	flavin mononucleotide	454.3	−3.30	195.3	7
1f8y	5-methyl-2′-deoxypseudouridine	282.2	−1.44	99.1	2
1ftx	{1-[(3-hydroxy-methyl-5-phosphonooxymethyl-pyridin-4-ylmethyl)-amino]-ethyl}-phosphonic acid	350.2	−5.24	161.6	6
1g2o	1,4-dideoxy-4-aza-1-(*S*)-(9-deazahypoxanthin-9-yl)-D-ribitol	267.3	−2.79	134.6	2
1gvo	2,4-dinitrophenol	183.1	1.65	114.7	2
1hjz	2-(*N*-morpholino)-ethanesulfonic acid	195.2	−2.55	64.9	3
1iei	zenarestat	440.6	3.21	80.8	4
1j4i	4-methyl-2-{[4-(toluene-4-sulfonyl)- thiomorpholine-3-carbonyl]-amino}-pentanoic acid	413.5	0.15	106.6	7
1ja9	pyroquilon	173.2	1.52	20.3	0
1jak	(2R,3R,4S,5R)-2-acetamido-3,4-dihydroxy-5-hydroxymethyl-piperidinium	205.2	−3.64	106.4	2
1kew	thymidine-5′-diphosphate	400.2	−4.26	185.8	6
1kkp	Ser-PLP[e]	331.2	−3.83	166.3	7
1kll	Gly-PLP[e]	301.2	−3.19	146.1	6
1kpg	*S*-adenosyl-L-homocysteine	384.4	−3.62	187.1	7
1kt7	Retinol	286.5	5.51	20.2	5
1l4g	nicotinate mononucleotide	333.2	−5.17	154.1	5
1l5k	1-alpha-D-ribofuranosyl-benzimiazole-5′-phosphate	329.2	−3.05	129.2	4
1l5l	7-alpha-D-ribofuranosyl-purine-5′-phosphate	331.2	−4.26	155.0	4
1l5m	7-alpha-D-ribofuranosyl-2-aminopurine-5′-phosphate	346.2	−4.68	181.0	4
1lc8	{3-[(3-hydroxy-2-methyl-5-phosphonooxymethyl-pyridin-4-ylmethyl)-amino]-2-methyl-propyl}-phosphonic acid	381.2	−4.36	167.6	8
1li4	neplanocin	261.2	−1.09	127.2	2
1lii	adenosine	267.2	−1.88	139.5	2
1m2g	adenosine-5-diphosphoribose	557.3	−6.59	285.2	9
1mm7	quisqualate	189.1	−3.58	126.4	3
1mqj	willardiine	199.2	−3.59	117.2	3
1mvc	4-[2-(5,5,8,8-tetramethyl-6,7-dihydronaphthalen-2-yl)-1,3-dioxolan-2-yl]benzoate (BMS649)	379.5	3.96	58.6	3
1n1t	2-deoxy-2,3-dehydro-*N*-acetyl-neuraminic acid	290.2	−4.40	159.4	5
1n3i	3-hydroxy-4-hydroxymethyl-1-(4-oxo-4,4a,5,7a-tetrahydro-3H-pyrrolo[3,2-d]pyrimidin-7-ylmethyl)-pyrrolidinium	265.3	−1.95	102.2	3
1nvr	staurosporine	467.5	4.00	74.03	2
1oh0	equilenin	266.3	3.94	37.3	0
1oio	*N*-acetyl-D-glucosamine	221.2	−3.08	119.3	2
1owe	6-[(Z)-amino(imino)methyl]-*N*-phenyl-2-naphthamide	290.3	1.56	80.7	3
1p4j	C-(1-hydrogyl-beta-D-glucopyranosyl) formamide	223.2	−4.37	153.5	2
1pfy	5′-O-[(L-methionyl)-sulfamoyl]adenosine	478.5	−3.36	219.4	9
1pg4	adenosine-5′-monophosphate-propyl ester	388.3	−2.04	171.9	7
1r0p	methyl(5S,6R,8R)-6-hydroxy-5-methyl-13-oxo-5,6,7,8,14,15-hexahydro-13H-5,8-epoxy-4b,8a,14-triazadibenzo[b,h]cycloocta[1,2,3,4-jkl]cyclopenta[e]-as-indacene-6-carboxylate (K-252A)	467.5	4.33	94.7	1
1sg0	resveratrol	228.2	2.97	60.7	2
1t40	2-[5-fluoro-2-[(4,5,7-trifluoro-1,3-benzothiazol-2-yl)methylcarbamoyl]phenoxy]ethanoic acid (IDD552)	413.3	3.26	91.4	6
1tkg	5′-O-(*N*-(L-seryl)-sulfamoyl)adenosine	434.4	−4.90	239.7	7
1uf5	*N*-carbamyl-D-methionine	191.2	−1.70	95.3	5
1urg	maltose	342.3	−5.40	189.5	4
1v7c	(2E)-2-[({3-hydroxy-2-methyl-5-[(phosphonooxy)methyl]pyridin-4-yl}methyl)amino]-5-phosphonopent-2-enoic acid	421.2	−4.78	197.3	10
1wap	L-tryptophan	204.2	−0.93	83.6	3
1wu6	xylobiose	282.2	−4.12	149.1	2
1xoz	tadalafil	389.4	2.31	74.9	1
1yki	nitrofurazone	198.1	0.19	126.4	3
2ay3	3-(3,4-dimethoxyphenyl)propionic acid	209.2	0.39	58.6	5
2prj	1-*N*-acetyl-beta-D-glucosamine	221.2	−3.08	119.3	2
2skc	glucose	180.2	−3.22	110.4	1

[a] Molecular weight. [b] The calculated log *P* value,[14] based on an atomic contribution model. [c] Polar surface area,[15] calculated using group contributions to approximate the polar surface area only from the connection table information. [d] Number of rotatable single bonds. Conjugated single bonds are not included. [e] PLP = pyridoxal phosphate.

atoms in the docked structure from the X-ray structure. For simplicity, the amino acids located within 6.0 Å from the non-hydrogen atoms of the small molecule were included in the calculations. The atomic coordinates of all atoms of the small molecule and hydrogen atoms of the selected amino acids were optimized. The dielectric constants were varied over a range of $\epsilon = 1-20$. In Figure 3, the effect of ϵ on the $N^+\cdots O^-$ distance is illustrated. The mean distances in 59

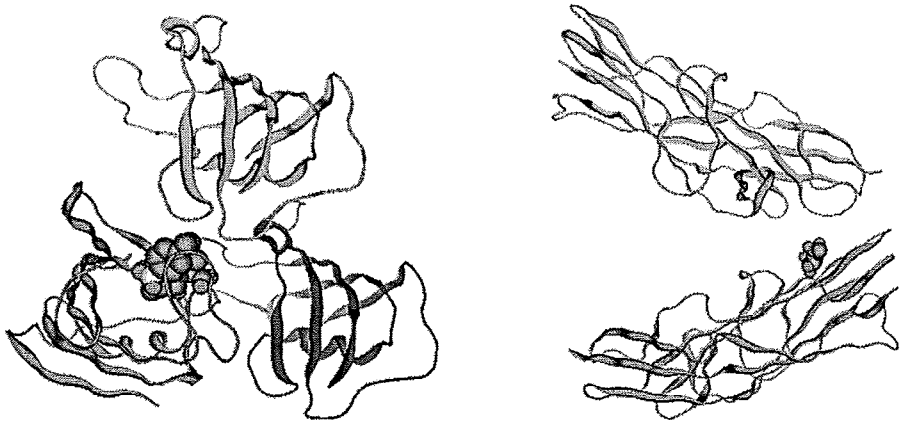

Figure 2. Small molecules entrapped between multiple proteins in the crystal structures.

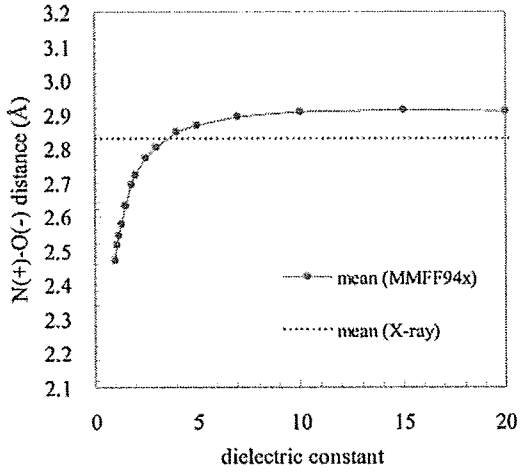

Figure 3. Effect of dielectric constant (ϵ) on the intermolecular $N^+\cdots O^-$ distances.

complex structures calculated using different values of ϵ were compared with the mean distance of 2.83 Å observed in 59 X-ray structures. If $\epsilon = 1.0$, the mean distance is <2.5 Å, and it is significantly shorter than that in the X-ray structures. The mean distance sharply increases with ϵ and approaches the experimental value. Above 7, it reaches a plateau. Judging from the curve, a dielectric constant of $\epsilon = 3-5$ is more preferable. It clearly suggests that ϵ values of <3 or >7 are not suitable, as long as we use MMFF94x as a potential function suite. We adopted a dielectric constant of $\epsilon = 5.0$ in this study. The balance of the absolute values of electrostatic and van der Waals interactions is generally a good rule of thumb to judge the validity of the nonbonded potential functions qualitatively. In Figure 4, the electrostatic and van der Waals interactions calculated with two different dielectric constants of 1.0 and 5.0 are compared. This figure shows the distribution of the values for 59 structures. Obviously, the balance is poor when 1.0 is applied for ϵ. The electrostatic interactions take mostly large negative values. On the other hand, the estimated van der Waals interactions are mostly positive. When 5.0 is applied for ϵ, however, the signs of the both interaction energy are mostly negative. It indicates that the ϵ value of 5.0 is more appropriate for the docking simulations. Since we apply a

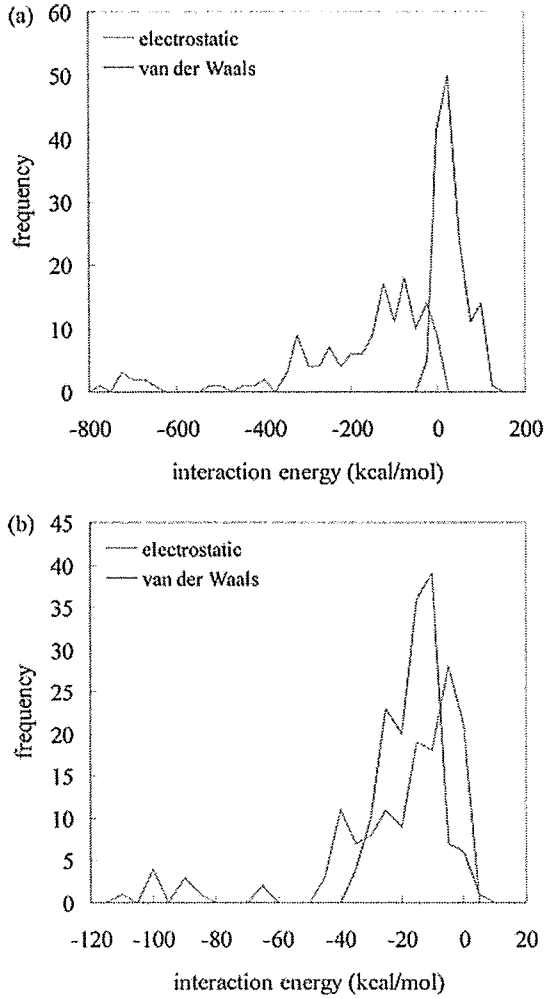

Figure 4. Effect of dielectric constant (ϵ) on the electrostatic and van der Waals interaction energies.

common dielectric constant for all 59 docking experiments, we thought further tuning of ϵ is not meaningful and 5.0 was used as the value of ϵ throughout this study. The relevance of this value can be validated by the docking performance.

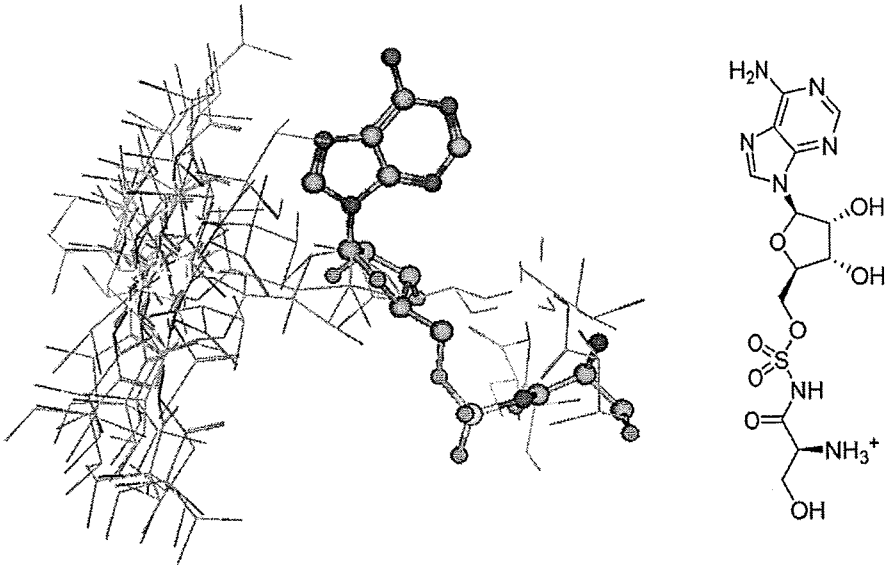

Figure 5. Ligand structures of 1TKG. Conformations generated by ASEDock (line) and the X-ray structure (ball-and-stick), as well as the chemical structure, are shown.

3. RESULTS AND DISCUSSION

3.1. Docking Results. A summary of the docking results is given in Table 1. In this study, the solution that gives the minimum U_{total} is assumed to be the best solution. The RMSD value that was used to evaluate the docking precision is derived from the best solution. The diffraction-component precision index (DPI) (hereafter denoted as σ) is "a good and rough guide" to coordinate the precision of experimentally obtained structures[16] and can be used to evaluate the reliability of the docking results. Suppose the standard uncertainty of the observed and predicted molecular model is the same in magnitude and is equal to σ, the estimated standard uncertainty of the RMSD between the corresponding non-hydrogen atoms in the observed and predicted molecules can be approximated to be $\sqrt{2}\sigma$.[7] The value of $2\sqrt{2}\sigma$ is given in this table as a guide of standard uncertainty of the RMSD. The RMSD values of 46 structures, which comprise ~78% of the entire dataset, are less than twice the corresponding estimated error of the observed structures. This indicates that the level of precision of the redocking results attained by ASEDock is mostly comparable to the expected experimental errors of the X-ray structures. An RMSD value of ≤2 Å is generally used as a rough guide to judge the correctness of the redocked structure. If we use this criterion as a measure of successful redocking, 58 out of 59 structures were redocked successfully. A success rate of ~98% was attained. This markedly high success rate demonstrates that if the high-quality X-ray structures of the complexes are available, ASEDock can precisely predict the dispositions and the structures of various small molecules at the concavities in the target proteins.

A dielectric constant of $\epsilon = 5.0$ was used in these docking experiments. The markedly good reconstruction of the X-ray structures strongly indicates that, in the concavities of these 59 structures, a dielectric constant of $\epsilon = 5.0$ is appropriate. Moreover, the high success rate of docking for various protein−ligand systems indicates that the dielectric constant of 5.0 should be generally acceptable in the docking simulation of druglike molecules at druggable concavities.

3.2. A Case of Failure. The redocking of 1TKG was in failure, and there may be multiple reasons for this failure. In Figure 5, the conformations of the ligand generated by ASEDock and the X-ray structure are compared. Obviously, ASEDock failed to generate a conformation that corresponds to the X-ray structure. The RMSD between the best generated conformation and the X-ray structure was 1.784 Å. The magnitude of the deviation seems to be beyond the radius of convergence by molecular mechanics calculations. However, it is intriguing that the very similar ligand of 1PFY was successfully redocked. In this case, an almost correct conformation with the RMSD of 0.906 Å was generated, as shown in Figure 6, and was successfully optimized to give the final RMSD of 0.504 Å. Although the ligand in 1TKG takes a more-folded conformation than that in 1PFY, most of the generated conformations are relatively extended. The generation method of conformation adopted in ASEDock is possibly slightly biased for this particular class of structure. It indicates that improvement of the method of conformation generation promises further improvement of the docking simulations.

3.3. Applications of ASEDock to the Structures for Which Ph4Dock Failed To Give Reasonable Answers. In our previous paper,[7] after a merging of the structures in a CCDC/Astex validation set[17] and a dataset proposed by Wang et al.,[18] we selected 43 structures for evaluation of Ph4Dock. Ph4Dock marked an appreciably good success rate of 86%, based on an rmsd of ≤2.0 Å, in redocking experiments. Nevertheless, Ph4Dock failed in redocking of six complexes, i.e., 1B9V, 1C1E, 1D3D, 1D3P, 1YEE, and 25C8. These structures are not included in the 59 structures, because they violate the criteria of the high quality used in this study. A summary of the docking results for these structures is given in Table 3. For all structures, the RMSDs were <2.0 Å, and the X-ray structures were reasonably reconstructed. The

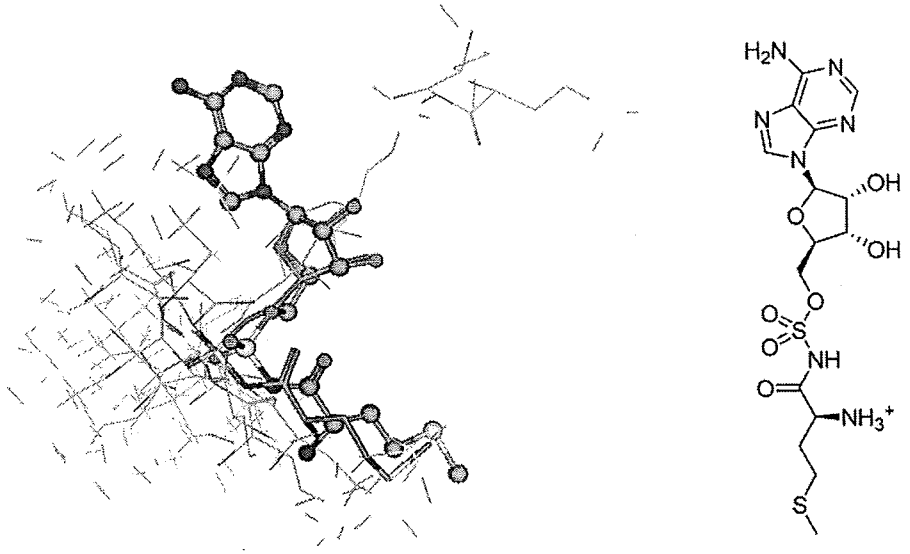

Figure 6. Ligand structures of 1PFY. Conformations generated by ASEDock (line) and the X-ray structure (ball-and-stick), as well as the chemical structure, are shown.

Table 3. Docking Results Obtained by ASEDock for 1B9V, 1C1E, 1D3D, 1D3P, 1YEE, and 25C8

PDB code	resolution (Å)	R_{free}	DPI (Å)	$2\sqrt{2}\sigma$ (Å)[a]	RMSD (Å)	lowest U_{total} (kcal/mol)
1B9V	2.35	0.271	0.467	1.321	0.945	48.6
1C1E	1.90	0.294	0.347	0.982	0.223	61.4
1D3D	2.04	0.223	0.288	0.815	1.940	62.4
1D3P	2.10	0.214	0.295	0.834	1.370	66.9
1YEE	2.20	0.260	0.141	0.398	0.993	−11.6
25C8	2.00	0.292	0.326	0.923	1.786	13.6

[a] $\sigma = \sigma(r, B_{avg})$.

RMSDs for 1B9V and 1C1E were $<2\sqrt{2}\sigma$, and their structures were rebuilt within experimental error. One example of the redocking results is shown for 1C1E in Figure 7. In this case, there are no hydrogen bonds between the ligand and the protein. This ligand is compact in shape and has no specific directionality. Therefore, it was difficult to pose the molecule in the concavity by Ph4Dock, which best uses pharmacophores as docking guides. As shown in this figure, the molecule well covers the portion where alpha spheres are densely populated. This example illustrates the crucial advantage of ASEDock that adapts the ASE score.

4. CONCLUSIONS

The successful redocking is an indispensable prerequisite to apply a docking algorithm to virtual screening of compounds that could specifically bind a target protein. In addition, such docking software is usually composed of several complex routines and a selection of appropriate parameters is important to obtain the optimum docking results. Therefore, the redocking experiments are essential in determining an appropriate set of parameters adapted to a particular problem.

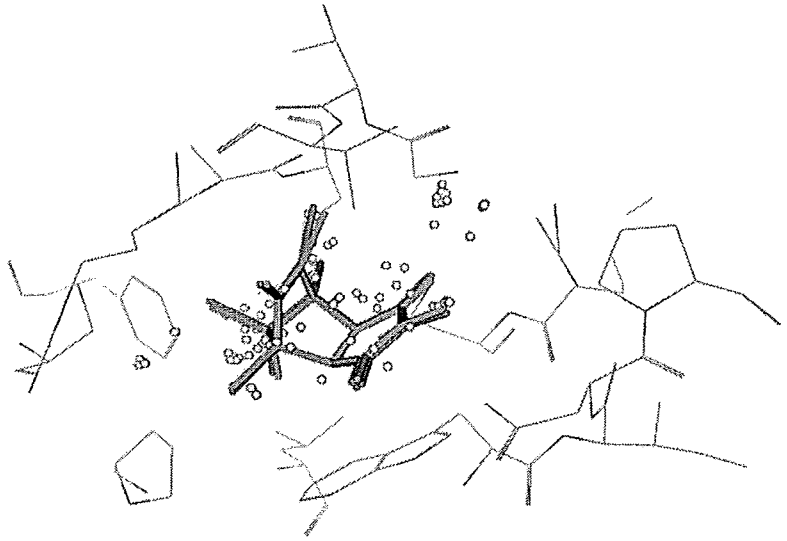

Figure 7. Redocked result of 1C1E. Alpha spheres calculated in the concavity are shown by small spheres. The ligand structure obtained by X-ray analysis and ASEDock are depicted by red and green sticks, respectively.

ASEDock is a novel docking program based on an accurate modeling of concavity shape and an effective function that evaluates the shape similarity between the model and the ligand. To evaluate the docking accuracy of ASEDock, redocking experiments for a selection of 59 highest-quality protein−ligand complexes from PDB were undertaken.

All the current docking algorithms involve several thorny problems, such as the quality of the potential functions, the accuracy of atomic charge, the generation of the ligand conformations, the effect of induced fit, and the effect of water molecules. Despite these inherent problems, however, the redocking performance of ASEDock is reasonably good, as far as the high-quality crystal structures are used. The markedly high success of ASEDock in redocking experiments clearly indicates that the most important factor governing the docking/binding process is shape complementarity.

ACKNOWLEDGMENT

This work was partially supported by the Grant-in-Aid for Scientific Research (A) (19200024) from MEXT (Ministry of Education, Culture, Sports, Science and Technology) for N.H.

REFERENCES AND NOTES

(1) Berman, H. M.; Westbrook, J.; Fenz, Z.; Gilliland, G.; Bhat, T. N.; Weissig, H.; Shindyalov, I. N.; Bourne, P. E. The protein data bank. *Nucleic Acids Res.* **2000**, *28*, 235−242.

(2) Rarey, M.; Kramer, B.; Lengauer, T.; Klebe, G. A fast flexible docking method using an incremental construction algorithm. *J. Mol. Biol.* **1996**, *261*, 470−489.

(3) Morris, G. M.; Goodsell, D. S.; Halliday, R. S.; Hey, R.; Hart, W. E.; Belew, R. K.; Olson, A. J. Automated docking using a Lamarckian genetic algorithm and an empirical binding free energy function. *J. Comput. Chem.* **1998**, *19*, 1639−1662.

(4) Jones, G.; Willett, P.; Glen, R. C.; Leach, A. R.; Taylor, R. Development and validation of a genetic algorithm for flexible docking. *J. Mol. Biol.* **1997**, *267*, 727−748.

(5) Friesner, R. A.; Banks, J. L.; Murphy, R. B.; Halgren, T. A. Glide: A New Approach for Rapid Accurate Docking and Scoring. 1. Method and Assessment of Docking Accuracy. *J. Med. Chem.* **2004**, *47*, 1739−1749.

(6) Jain, A. N. Surflex: Fully Automatic Molecular Docking Using a Molecular Similarity-Based Search Engine. *J. Med. Chem.* **2003**, *46*, 499−511.

(7) Goto, J.; Kataoka, R.; Hirayama, N. Ph4Dock:Pharmacophore-Based Protein-Ligand Docking. *J. Med. Chem.* **2004**, 47, 6804−6811.

(8) MOE (Molecular Operating Environment), Version 2004.0301; Chemical Computing Group, Inc.: Montreal, Quebec, Canada, 2006.

(9) Wojciechowski, M.; Lesyng, B. Generalized Born Model: Analysis, Refinement and Applications to Proteins. *J. Phys. Chem. B* **2004**, *B108*, 18368−18376.

(10) Halgren, T. A. Merck molecular force field. I. Basis, form, scope, parameterization, and performance of MMFF94. *J. Comput. Chem.* **1996**, *17*, 490−519.

(11) Edelsbrunner, H.; Facello, M.; Fu, P.; Liang, J. Measuring Proteins and Voids in Proteins. In *Proceedings of the 28th Hawaii International Conference on System Sciences (HICSS'95)*; Institute of Electrical and Electronics Engineers (IEEE): Piscataway, NJ, 1995; Vol. 5, pp 256−264.

(12) Kearsley, S. K.; and Smith, G. M. An Alternative Method for the Alignment of Molecular Structures: Maximizing Electrostatic and Steric Overlap. *Tetrahedron Comput. Methodol.* **1990**, *3*, 615−633.

(13) Horio, K.; Goto, J.; Muta, H.; Hirayama, N. A Simple Method to Improve the Odds in Finding 'Lead-like' Compounds from Chemical Libraries. *Chem. Pharm. Bull.* **2007**, *55*, 980−984.

(14) Wildman, S. A.; Crippen, G. M. Prediction of Physicochemical Parameters by Atomic Contributions. *J. Chem. Inf. Comput. Sci.* **1999**, *39*, 868−873.

(15) Ertl, P.; Rohde, B.; Selzer, P. Fast Calculation of Molecular Polar Surface Area as a Sum of Fragment-Based Contributions and Its Application to the Prediction of Drug Transport Properties. *J. Med. Chem.* **2000**, *43*, 3714−3717.

(16) Blow, D. M. A rearrangement of Cruickshank's formulae for the diffraction-component precision index. *Acta Crystallogr., Sect. D: Biol. Crystallogr.* **2002**, *D58*, 792−797.

(17) Cambridge Crystallographic Data Centre. hhtp:/www.ccdc.cam.ac.uk/products/life_sciences/validate/astex/pdb_entries (accessed July 10, 2004).

(18) Wang, R.; Lu, Y.; Wang, S. Comparative Evaluation of 11 Scoring Functions for Molecular Docking. *J. Med. Chem.* **2003**, *46*, 2287−2303.

CI700352Q

Single Injection of a Sustained-release Prostacyclin Analog Improves Pulmonary Hypertension in Rats

Hiroaki Obata[1,2], Yoshiki Sakai[3], Shunsuke Ohnishi[1], Satoshi Takeshita[4], Hidezo Mori[5], Makoto Kodama[2], Kenji Kangawa[6], Yoshifusa Aizawa[2], and Noritoshi Nagaya[1,4]

[1]Department of Regenerative Medicine and Tissue Engineering, National Cardiovascular Center Research Institute, Osaka, Japan; [2]Division of Cardiology, Niigata University Graduate School of Medical and Dental Science, Niigata, Japan; [3]Ono Pharmaceutical Co. Ltd., Research Headquarters, Osaka, Japan; [4]Department of Internal Medicine, National Cardiovascular Center, Osaka, Japan; [5]Department of Cardiac Physiology, National Cardiovascular Center Research Institute, Osaka, Japan; and [6]Department of Biochemistry, National Cardiovascular Center Research Institute, Osaka, Japan

Rationale: Although prostacyclin is recognized as a therapeutic breakthrough for pulmonary hypertension, it needs continuous infusion because of its short action. Therefore, we developed a new drug delivery system for prostacyclin. We prepared ONO-1301MS, a novel sustained-release prostacyclin analog polymerized with poly(D, L-lactic-co-glycolic acid) (PLGA) microspheres.

Objectives: We examined whether ONO-1301MS attenuates monocrotaline (MCT)-induced pulmonary hypertension in rats, and attempted to elucidate the underlying mechanisms responsible for the beneficial effects of ONO-1301MS.

Methods: After MCT injection, rats were randomized to receive a single subcutaneous injection of 100 mg/kg ONO-1301MS or vehicle.

Measurements and Main Results: We prepared ONO-1301MS, which was polymerized with PLGA to release ONO-1301 for 3 weeks. A single administration of ONO-1301MS achieved sustained elevation of its circulating level and plasma cyclic adenosine 3′,5′-monophosphate level for 3 weeks, and attenuated an increase in a metabolite of thromboxane A_2 level. Rats had developed pulmonary hypertension 3 weeks after MCT injection; however, treatment with ONO-1301MS significantly attenuated the increases in right ventricular systolic pressure and right ventricular weight to body weight ratio. ONO-1301MS significantly inhibited hypertrophy of pulmonary arteries. Phosphorylation of extracellular signal-regulated protein kinase (ERK) in the lung was significantly increased in the control group, whereas this increase was markedly attenuated by treatment.

Conclusions: We developed a new drug delivery system for prostacyclin using PLGA and ONO-1301. A single injection of ONO-1301MS resulted in sustained activity for 3 weeks, and attenuated pulmonary hypertension, partly through its antiproliferative effect on vascular smooth muscle cells via inhibition of ERK phosphorylation.

Keywords: pulmonary hypertension; prostacyclin analog; sustained-release preparation; extracellular signal regulated kinase; poly(lactic-co-glycolic acid)

AT A GLANCE COMMENTARY

Scientific Knowledge on the Subject

Although prostacyclin is recognized as a therapeutic breakthrough for pulmonary hypertension, it needs continuous infusion because of its short action. For patients with pulmonary hypertension, development of a sustained-release prostacyclin would be beneficial in terms of stable hemodynamics and quality of life.

What This Study Adds to the Field

A single injection of ONO-1301MS resulted in sustained activity for 3 weeks, and attenuated pulmonary hypertension in rats.

Pulmonary arterial hypertension is a rare but life-threatening disease characterized by progressive pulmonary hypertension that leads to right ventricular (RV) failure and death (1). Prostacyclin, a metabolite of arachidonic acid, has vasoprotective effects, including vasodilation, antiplatelet aggregation, and inhibition of smooth muscle cell (SMC) proliferation (2–4). Thus, continuous intravenous infusion of prostacyclin (epoprostenol) has become recognized as a therapeutic breakthrough for pulmonary arterial hypertension (5–7). The dramatic success of long-term intravenous prostacyclin has led to the development of prostacyclin analogs (8–11). Nevertheless, treatment with prostacyclin or its analogs has some problems in the clinical setting. Epoprostenol therapy requires a continuous intravenous infusion device, and is therefore more invasive and uncomfortable than taking prostacyclin analogs. On the other hand, prostacyclin analogs, such as subcutaneously infused treprostinil, inhaled iloprost, and oral beraprost, need continuous infusion or frequent administration because of their short duration of action (5–11). In fact, epoprostenol has a very short half-life (<6 min) (12), treprostinil has been reported to have a half-life of 4.6 hours after cessation of continuous subcutaneous infusion (13), iloprost has a serum half-life of 20 to 25 minutes, and the elimination half-life of beraprost is 35 to 40 minutes after oral administration (12).

Recently, we developed a new type of prostacyclin agonist, ONO-1301 (Figure 1), which has long-lasting prostacyclin activity and an inhibitory effect on thromboxane synthase (14). ONO-1301 does not contain prostanoid structures, such as a five-membered ring or allylic alcohol, which are digested by 15-hydroxyprostaglandin dehydrogenase (Figure 1). These structures are considered to be crucial for the stable activity of ONO-1301. This agent is metabolized by cytochrome P450, and the half-life was about 5.6 hours in our previous study (14). In

(*Received in original form March 1, 2007; accepted in final form October 26, 2007*)

Supported by research grants from Ono Pharmaceutical Co., Ltd. (no. 526); Human Genome Tissue Engineering 009 from the Ministry of Health, Labor, and Welfare; the Program for Promotion of Fundamental Studies in Health Science of the National Institute of Biomedical Innovation (NIBIO); and a Grant-in-Aid for Exploratory Research from the Ministry of Education, Culture, Sports, Science, and Technology.

Correspondence and requests for reprints should be addressed to Noritoshi Nagaya, M.D., Department of Regenerative Medicine and Tissue Engineering, National Cardiovascular Center Research Institute, 5-7-1 Fujishirodai, Suita, Osaka 565-8565, Japan. E-mail: nnagaya@ri.ncvc.go.jp

This article contains an online supplement, which is accessible from this issue's table of contents at www.atsjournals.org

Am J Respir Crit Care Med Vol 177. pp 195–201, 2008
Originally Published in Press as DOI: 10.1164/rccm.200703-349OC on November 1, 2007
Internet address: www.atsjournals.org

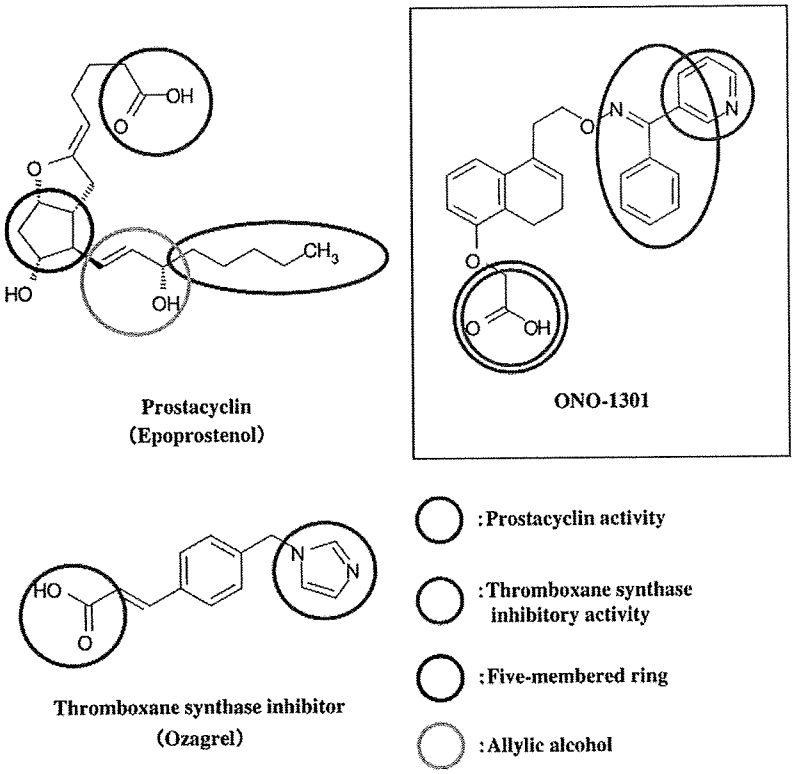

Figure 1. Chemical structures of ONO-1301, epoprostenol (prostacyclin analog), and ozagrel (thromboxane synthase inhibitor). Epoprostenol shares common characteristics with prostanoid structures, including a five-membered ring and an allylic alcohol (*blue* and *yellow circles*, respectively). In contrast, ONO-1301 has a carboxylic acid and a lipid-soluble functional group that activates the prostacyclin receptor (*green circles*), but does not have prostanoid structures, which allow long-lasting prostacyclin activity. Unlike epoprostenol, ONO-1301 has thromboxane synthase inhibitory activity because of a 3-pyridine radical and carboxylic acid within its molecule (*red circles*), similar to ozagrel.

addition, ONO-1301 has a 3-pyridine radical, which is known to inhibit thromboxane synthase through interaction with carboxylic acid via a hydrogen bond (Figure 1). Repeated administration of ONO-1301 attenuated monocrotaline (MCT)-induced pulmonary hypertension and improved survival in rats. Although the half-life of plasma ONO-1301 concentration is longer than that of any other prostacyclin analogs, ONO-1301 still needs to be administered twice a day subcutaneously to achieve a significant improvement in pulmonary hypertension. For patients with pulmonary hypertension, development of a long-acting, sustained-release prostacyclin analog would be beneficial in terms of stable hemodynamics and quality of life. To overcome these problems, we developed a new drug delivery system for prostacyclin. We prepared a novel sustained-release prostacyclin analog polymerized with poly(D,L-lactic-co-glycolic acid) (PLGA) microspheres (ONO-1301MS). PLGA microspheres, which are biodegradable and biocompatible compounds, have been used as a controlled delivery system for proteins and drugs (15–20). The release of drug from PLGA microspheres occurs through degradation of the polymeric matrix. Here, we showed that a single subcutaneous administration of ONO-1301MS achieved sustained elevation of its circulating level for 3 weeks.

Thus, the purposes of this study were as follows: (*1*) to investigate whether a single subcutaneous administration of ONO-1301MS attenuates MCT-induced pulmonary hypertension in rats and (*2*) to elucidate the underlying mechanisms responsible for the beneficial effects of this compound.

METHODS

Preparation of ONO-1301MS

ONO-1301MS is polymerized ONO-1301 with PLGA microspheres. ONO-1301 and PLGA (polylactic acid to glycolic acid ratio of 50:50) were dissolved in dichloromethane. The dissolved polymer was added to polyvinyl alcohol aqueous solution to form an oil-in-water emulsion. Then, dichloromethane was evaporated by stirring. After centrifugation and washing, ONO-1301MS was isolated by lyophilization.

Morphologic Studies by Scanning Electron Microscopy

To evaluate the shape and surface morphology of ONO-1301MS, we used a scanning electron microscope (model S-2460N; Hitachi, Tokyo, Japan). After lyophilization, the microspheres were mounted on an aluminum stub and coated with a thin layer (200 Å) of gold by an ion sputter (model E-1010; Hitachi). The surface morphology of the microsphere samples was then visualized under a scanning electron microscope.

Particle Diameter

ONO-1301MS was suspended in distilled water and dispersed by sonication. The particle diameter was measured by a laser diffraction particle size analyzer (model SALD-2100; Shimadzu, Kyoto, Japan).

Encapsulation Efficiency

Acetonitrile containing n-propyl 4-hydroxybenzoate served as an internal control to obtain the encapsulation efficiency, and this solution was homogenized by a sonicator. The concentration of ONO-1301 in this solution was analyzed by high-performance liquid chromatography (HPLC). The encapsulation efficiency was calculated as follows:

$$\text{Encapsulation efficiency}(\%) = (\text{measured value}/\text{theoretical value}) \times 100.$$

In Vitro Release of ONO-1301 from PLGA Microspheres

ONO-1301MS was suspended in phosphate-buffered saline (0.067 mol/L salt concentration, pH 6.8) containing 0.2% Tween-80 to adjust the concentration of ONO-1301 to 100 μg/ml. This solution was aliquoted into 1 ml and incubated at 37°C. At various time intervals, one of the aliquots was centrifuged for 5 minutes at 12,000 rpm. The supernatant was discarded, the pellet was dissolved in acetonitrile, and the remaining amount of ONO-1301 was analyzed by HPLC.

Animal Models

We used 5-week-old male Wistar rats weighing 95 to 110 g. The rats were randomly given a subcutaneous injection of either 60 mg/kg MCT or 0.9% saline, and assigned to receive a subcutaneous injection of 100 mg/kg ONO-1301MS or 0.9% saline. This protocol resulted in the creation of three groups: normal rats given 0.9% saline (sham group, n = 10), MCT rats given 0.9% saline (control group, n = 11), and MCT rats treated with ONO-1301 MS (treated group, n = 11). We chose the maximum dose that did not induce significant hypotension (*see* Figure E1 in the online supplement).

In Vivo Experimental Protocol

After anesthetization by an intraperitoneal injection of 30 mg/kg pentobarbital, rats were given a subcutaneous injection of either 60 mg/kg MCT or 0.9% saline. Subsequently, rats received a single subcutaneous injection of 100 mg/kg ONO-1301MS or 0.9% saline. ONO-1301MS was suspended with 0.9% saline containing 0.2% Tween-80. Hemodynamic measurements and histologic analyses were performed on Day 21. For hemodynamic measurements, rats were anesthetized by intraperitoneal injection of 20 mg/kg pentobarbital, and the following indexes were recorded after an equilibration period. A polyethylene catheter (model PE-50; BD Biosciences, San Jose, CA) was inserted into the right carotid artery to measure heart rate and mean arterial pressure. The catheter was inserted through the right jugular vein into the right ventricle for the measurement of RV pressure. The values of heart rate, mean arterial pressure, and systolic RV pressure were calculated from a series of 20 consecutive heart beats in each rat. Finally, cardiac arrest was induced by injection of 2 mmol/L potassium chloride through the catheter. The ventricles and lungs were excised, dissected free, and weighed. The RV weight to body weight ratio (RV/BW), left ventricular plus septal weight to body weight ratio (LV + S/BW), and RV weight to left ventricular plus septal weight ratio (RV/LV + S) were calculated as indexes of ventricular hypertrophy, as reported previously (21). All protocols were performed in accordance with the guidelines of the Animal Care Ethics Committee of the National Cardiovascular Center Research Institute (Osaka, Japan).

Morphometric Analysis of Pulmonary Arteries

Paraffin sections of 4-μm thickness were obtained from the lower region of the right lung and stained with hematoxylin and eosin. Analysis of the medial wall thickness of the pulmonary arteries was performed as described previously (22). In brief, the external diameter and the medial wall thickness were measured in 20 muscular arteries (25–100-μm external diameter) per lung section. For each artery, the medial wall thickness was expressed as follows:

$$\%\ \text{wall thickness} = ([\text{medial thickness} \times 2]/\text{external diameter}) \times 100$$

A lung section was obtained from individual rats for comparison among the three groups (n = 5 in each group).

Assay of Plasma Levels of ONO-1301 and Cyclic AMP

To investigate whether a single subcutaneous administration of ONO-1301MS produces long-lasting prostacyclin activity in rats, we measured plasma levels of ONO-1301 and cyclic AMP (cAMP) after ONO-1301MS injection. Fourteen rats were assigned to receive a single subcutaneous injection of 100 mg/kg ONO-1301MS or 0.9% saline (n = 7 in each group), and blood was drawn from the tail vein on Days 0, 7, 14, and 21. Blood was immediately transferred to a chilled glass tube containing 1 mg/ml disodium ethylenediaminetetraacetic acid and 500 U/ml aprotinin, and centrifuged immediately. Plasma ONO-1301 level was measured by liquid chromatography tandem mass spectrometry assay. Plasma cAMP level was measured with a radioimmunoassay kit (cAMP assay kit; Yamasa Co., Chiba, Japan), as reported previously (23).

Assay of Urinary Level of 11-Dehydro Thromboxane B_2

To investigate the effect of ONO-1301MS on thromboxane synthesis in rats, we measured urinary level of 11-dehydro thromboxane B_2 (11-$DTXB_2$), a metabolite of thromboxane A_2 (TXA_2), after single subcutaneous injection of ONO-1301MS (100 mg/kg) or vehicle (n = 8 in each group). Urine samples were collected for 24 hours on Day 14 by using metabolic cages, and urinary concentration of 11-$DTXB_2$ was measured with an enzyme immunoassay kit (11-$DTXB_2$ assay kit; Cayman Chemical Co., Ann Arbor, MI). The urinary level of 11-$DTXB_2$ was expressed as the ratio of urinary 11-$DTXB_2$ concentration to that of creatinine, as reported previously (24).

Western Blot Analysis

To investigate the effect of ONO-1301MS on proliferative signaling pathways in homogenized lung tissue, the protein expression of extracellular signal-regulated protein kinase (ERK) 1/2 and phospho-ERK1/2 was determined by Western blotting. Western blotting was performed using rabbit monoclonal antibodies raised against ERK1/2 and phospho-ERK1/2 (Cell Signaling Technology, Danvers, MA). Peripheral samples of lung tissue were obtained on Day 21 from individual rats for comparison among the three groups (n = 6 in each group). Positive protein bands were visualized by means of chemiluminescence (enhanced chemiluminescence kit; Amersham Biosciences, Little Chalfont, UK). Western blot analysis using a mouse polyclonal antibody raised against β-actin (Sigma Chemical Corp., St. Louis, MO) was used as a protein loading control. The resultant bands were quantified using Image J 1.36 imaging software (National Institutes of Health; http://rsb.info.nih.gov/ij/).

Statistical Analysis

All data were expressed as mean ± SEM. Comparisons of parameters among the three groups were made by one-way analysis of variance (ANOVA), followed by Newman-Keuls test. Comparisons of the time course of parameters between the two groups were made by two-way ANOVA for repeated measures, followed by Newman-Keuls test. A value of $P < 0.05$ was considered statistically significant.

RESULTS

Characterization of ONO-1301MS

We prepared three kinds of ONO-1301MS (samples 1, 2, and 3). The external surface morphology of ONO-1301MS (sample 2 as a representative sample) exhibited a spherical shape with a smooth and uniform surface (Figure 2A). The particle size in samples 1, 2, and 3 was 21.2, 42.0, and 71.1 μm, respectively (Figure 2B; sample 2 as a representative sample). Encapsulation efficiency in each sample was 5.1, 21.8, and 17.4%, respectively. *In vitro*, each sample had different time periods of ONO-1301 release at 2, 3, and 4 weeks, respectively (Figure 2C). These data suggest that we were able to vary the release period of ONO-1301.

Long-lasting Activity of ONO-1301MS

To investigate the pharmacokinetics *in vivo*, we measured plasma ONO-1301 level after a single subcutaneous administration of ONO-1301MS, which was designed to release ONO-1301 for 3 weeks (sample 2). ONO-1301 was detected in plasma for 3 weeks, whereas plasma ONO-1301 level at baseline in the ONO-1301MS group and at all times in the vehicle group was below the detection limit (Figure 3A). In addition, plasma cAMP level after a single subcutaneous administration of ONO-1301MS was significantly higher than that in the control group (Figure 3B). Interestingly, the increase in plasma cAMP level lasted for over 2 weeks in parallel with the change in plasma ONO-1301MS level (Figure 3). These results suggest that subcutaneous administration of ONO-1301MS achieves long-lasting activity in rats.

Inhibitory Effect of ONO-1301MS on Thromboxane Synthase

Urinary level of 11-$DTXB_2$ was markedly elevated 14 days after MCT injection (Figure 4). However, treatment with ONO-1301MS significantly decreased urinary level of 11-$DTXB_2$ in MCT rats. These results suggest that ONO-1301MS has a sustained inhibitory effect on thromboxane synthase activity.

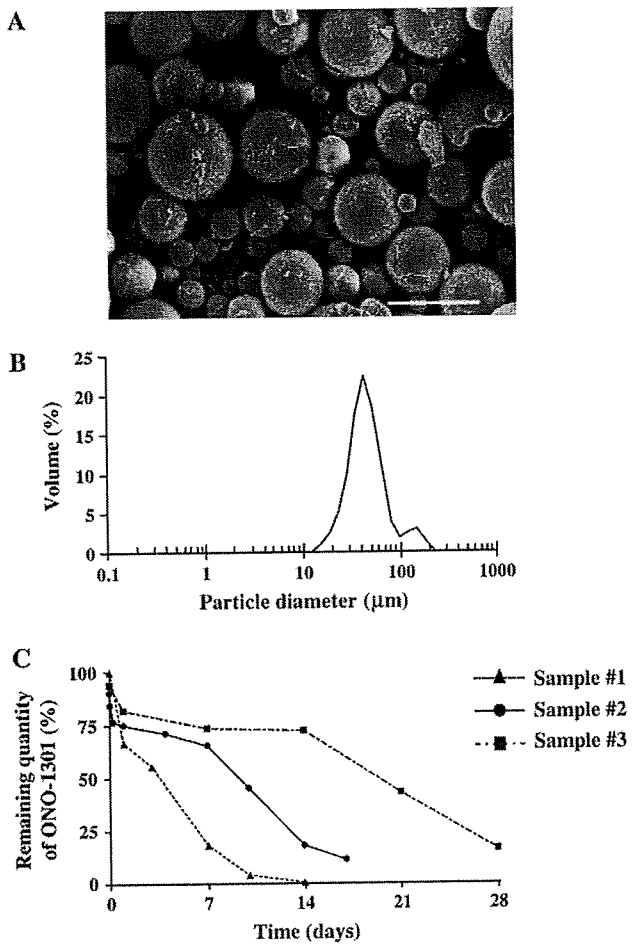

Figure 2. Physicochemical characteristics and *in vitro* release of ONO-1301. (*A*) Morphology of ONO-1301MS (sample 2) studied by scanning electron microscopy. *Scale bar* = 50 μm. (*B*) Particle diameter of ONO-1301MS (sample 2) obtained by a laser diffraction particle size analyzer. (*C*) Release profiles of ONO-1301MS in each sample.

Effects of ONO-1301MS on Pulmonary Hemodynamics and Vascular Remodeling

Three weeks after MCT injection, RV systolic pressure was markedly increased (Figure 5). However, the increase in RV systolic pressure was significantly attenuated in the treated group. Similarly, the increases in RV/BW and RV/LV + S in MCT rats were significantly attenuated by treatment with ONO-1301MS (Figure 5). There were no significant differences in heart rate or mean arterial pressure among the three groups (Table 1). Histologic examination demonstrated that hypertrophy of the pulmonary vascular wall was attenuated in the treated group compared with that in the control group (Figure 6).

No adverse reactions, such as flushing, diarrhea, or hypotension, were observed in the treated group, and there were no significant differences in blood biochemical markers of liver and renal function among the three groups (mean value ± SEM in sham, control, and treated group were, respectively: 139 ± 14, 145 ± 20, and 102 ± 12 IU/L in aspartate aminotransferase; 53 ± 3, 54 ± 5, and 45 ± 3 IU/L in alanine aminotransferase; 0.1 ± 0, 0.1 ± 0, and 0.1 ± 0 mg/dl in total bilirubin; 16.2 ± 1.1, 16.2 ± 0.4, and 15.4 ± 1.2 mg/dl in urea nitrogen; 0.22 ± 0.01, 0.21 ± 0.01, and 0.21 ± 0.01 mg/dl in creatinine; n = 5 in each group.). Moreover, no abnormality was observed at the injection site.

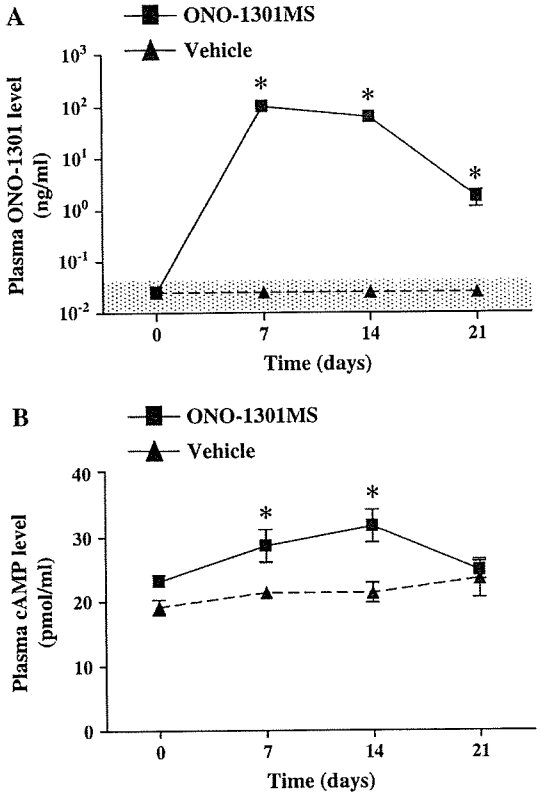

Figure 3. Time course changes in plasma ONO-1301 and cAMP. (*A*) Plasma ONO-1301 concentration after a single subcutaneous administration of ONO-1301MS or vehicle. The *shaded area* indicates below the lower limit of quantification (0.025 ng/ml) and is treated as 0 in the statistical analysis. (*B*) Changes in plasma cAMP level after a single subcutaneous administration of ONO-1301 MS or vehicle. Data are mean ± SEM. *$P < 0.05$ versus vehicle.

Inhibitory Effect of ONO1301-MS on Proliferative Signals

To investigate the effect of ONO1301-MS on proliferative signals in the lung, Western blot analyses were performed. There were no significant differences in the expression of ERK1 and ERK2 among the three groups (Figure 7). However, phosphorylation of ERK1 and ERK2 was significantly increased in the control group, whereas these increases were markedly attenuated in the treatment group (Figure 7).

DISCUSSION

In the present study, we demonstrated that (*1*) a novel sustained-release prostacyclin analog polymerized with PLGA

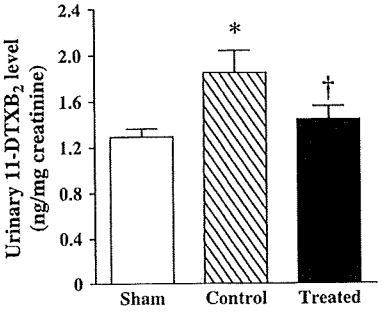

Figure 4. Effect of ONO-1301MS on thromboxane synthesis. Changes in urinary 11-dehydro thromboxane B_2 (11-DTXB_2) level on Day 14. Sham = sham rats given vehicle; control = monocrotaline (MCT)-treated rats given vehicle; treated = MCT rats treated with ONO-1301MS. Data are mean ± SEM. *$P <$ 0.05 versus sham; †$P <$ 0.05 versus control.

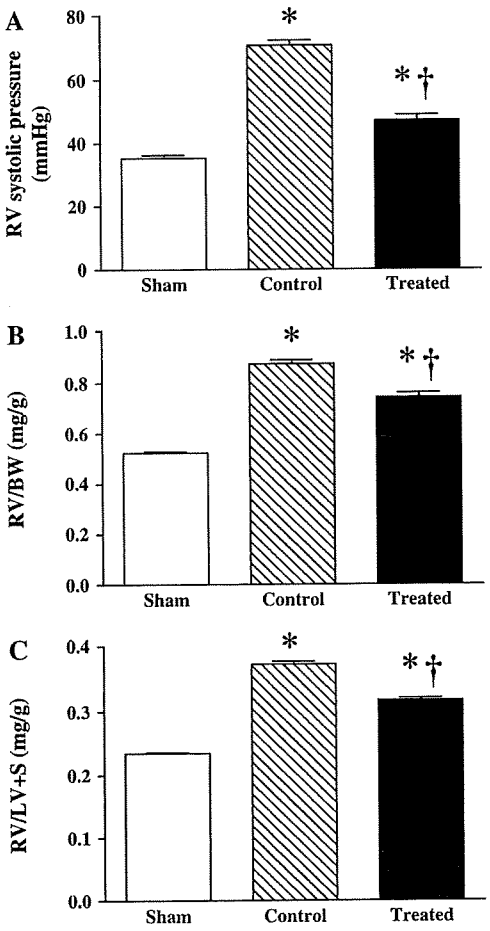

Figure 5. Effects of ONO-1301MS on pulmonary hemodynamics. (*A*) Effects of ONO-1301MS on right ventricular (RV) systolic pressure, (*B*) RV weight to body weight (RV/BW), and (*C*) RV weight to left ventricular plus septal weight (RV/LV + S). Sham = sham rats given vehicle; control = monocrotaline (MCT)-treated rats given vehicle; treated = MCT rats treated with ONO-1301MS. Data are mean ± SEM. $^*P < 0.05$ versus sham; $^\dagger P < 0.05$ versus control.

microspheres (ONO-1301MS) allowed a 3-week elevation of its circulating level, (2) ONO-1301MS had a sustained inhibitory effect on thromboxane synthase activity, and (3) a single subcutaneous administration of ONO-1301MS attenuated MCT-induced pulmonary hypertension in rats.

TABLE 1. PHYSIOLOGIC PROFILES OF THREE EXPERIMENTAL GROUPS

	Sham*	Control†	Treated‡
No. of rats	10	11	11
BW, g	203 ± 4	165 ± 7§	175 ± 3§
Heart rate, beats/min	454 ± 7	441 ± 10	445 ± 6
Mean arterial pressure, mm Hg	110 ± 2	111 ± 3	107 ± 2
LV + S/BW, mg/g	2.23 ± 0.02	2.34 ± 0.02§	2.34 ± 0.04§

Definition of abbreviations: BW = body weight; LV = left ventricle; LV + S/BW = LV plus septal weight to body weight ratio.

Data are mean ± SEM. These measurements were performed on Day 21.

* Sham = rats given vehicle.

† Control = MCT rats given vehicle.

‡ Treated = MCT rats treated with ONO-1301MS.

§ $P < 0.05$ versus sham.

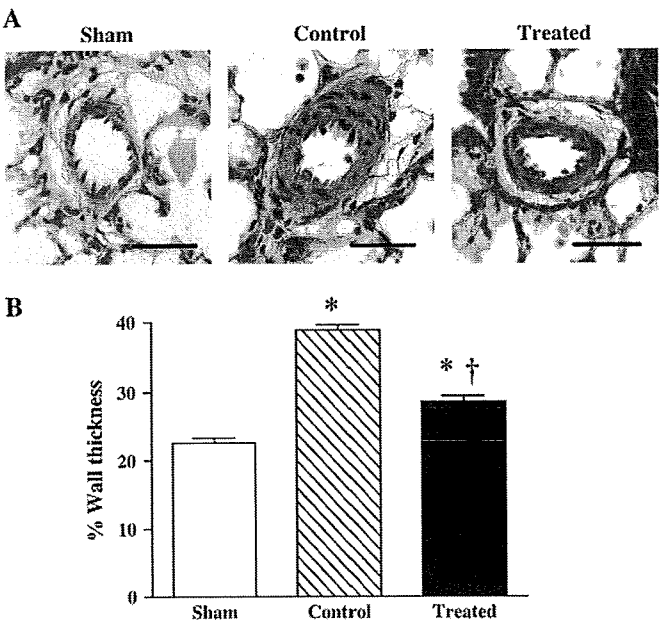

Figure 6. Effect of ONO-1301MS on vascular remodeling. (*A*) Representative photomicrographs of peripheral pulmonary arteries on Day 21. *Scale bars* = 50 μm. (*B*) Quantitative analysis of percentage of wall thickness in peripheral pulmonary arteries. Data are mean ± SEM. $^*P < 0.05$ versus sham; $^\dagger P < 0.05$ versus control.

Conventional prostacyclin and its analogs need continuous infusion or frequent administration because of their short duration of action. Previously, we reported a new type of prostacyclin agonist, ONO-1301, which has long-lasting prostacyclin activity and an inhibitory effect on thromboxane synthase (14). Although ONO-1301 has such interesting features, it still needs to be administered twice a day to achieve a significant improvement in pulmonary hypertension. To overcome this problem, we developed a new drug delivery system for prostacyclin. We polymerized ONO-1301 with PLGA microspheres to develop a novel sustained-release prostacyclin analog.

PLGA microspheres have been used as a controlled delivery system for bioactive agents (25). The release of bioactive agents from PLGA microspheres occurs through hydrolytic degradation of the polymeric matrix. Importantly, PLGA has already been used in humans. PLGA microspheres containing leuprorelin, a potent luteinizing hormone–releasing hormone analog, have been administered to patients with prostate and breast cancer by subcutaneous injection (26, 27). The rate of release of contents of PLGA microspheres can be changed by varying the factors affecting the hydrolytic degradation behavior of PLGA, such as lactate acid to glycolic acid ratio, average molecular weight of PLGA, and particle size (25). In the present study, we could control the degradation rate of ONO-1301MS. ONO-1301MS was designed to release ONO-1301 for 3 weeks, because it takes 3 weeks to induce pulmonary hypertension in rats after MCT injection. The present study demonstrated that the contained ONO-1301 was released for 3 weeks *in vitro*, producing a 3-week elevation of its circulating level after a single administration *in vivo*. It should be noted that only a single subcutaneous administration of ONO-1301MS attenuated MCT-induced pulmonary hypertension in rats. Thus, it might be possible to extend the administration interval for ONO-1301MS considerably longer than that with current prostacyclin analogs, and this could improve the quality of life in patients with pulmonary hypertension.

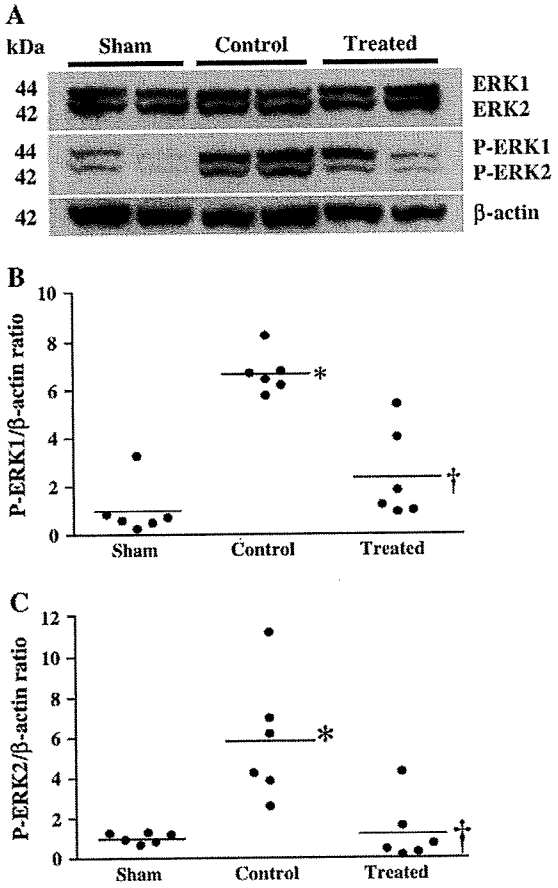

Figure 7. Effect of ONO-1301MS on extracellular signal-regulated protein kinase (ERK) phosphorylation. (*A*) Representative Western blotting for ERK, phospho-ERK (P-ERK) and β-actin (protein loading control) in lungs on Day 21 (n = 6 in each group). (*B* and *C*) Scatter plot of quantitative analysis of P-ERK expression in lung tissue. *Horizontal lines* in this figure show the mean value. $^{*}P < 0.05$ versus sham; $^{\dagger}P < 0.05$ versus control.

With regard to cAMP, which is a second messenger of prostacyclin and its analogs, it has been reported that plasma cAMP level remained increased after administration of prostacyclin analogs (23, 28). In our results, administration of ONO-1301MS increased the plasma cAMP level for over 2 weeks. This increase in plasma cAMP level was parallel to the change in plasma ONO-1301 level. In addition, ONO-1301MS attenuated the increase in urinary 11-$DTXB_2$ level in MCT rats 14 days after single administration. These results support that a single administration of ONO-1301MS produced a sustained beneficial effect for 3 weeks.

In the present study, we chose the maximum dose that did not induce significant hypotension. We did dose–response studies using ONO-1301MS (30, 100, and 300 mg/kg, respectively) (*see* Figure E1). ONO-1301MS at 300 mg/kg has induced significant hypotension. In addition, ONO-1301MS at 30 mg/kg did not significantly decrease RV systolic pressure (*see* Figure E3). On the other hand, ONO-1301MS at 100 mg/kg significantly decreased RV systolic pressure without significant hypotension. Furthermore, a single injection of 100 mg/kg ONO-1301 without PLGA or PLGA without ONO-1301 to MCT rats did not influence hemodynamics and vascular remodeling (*see* Figures E1–E3). These results suggest that a single injection of ONO-1301MS ameliorates MCT-induced pulmonary hypertension. Consistent with these hemodynamic data, RV/BW and medial wall thickness of pulmonary arteries, as indexes of RV hypertrophy and elevation of pulmonary arteriolar resistance, respectively, were significantly attenuated by the treatment with ONO-1301MS.

In histologic analysis, hypertrophy of pulmonary vessels after MCT injection was significantly attenuated by treatment with ONO-1301MS. An earlier clinical trial has shown that long-term therapy with epoprostenol significantly reduces pulmonary vascular resistance in patients who have no short-term response to vasodilators (5). It is speculated that such a beneficial effect of epoprostenol is caused not only by vasodilatation and antiplatelet aggregation but also by an antiproliferative effect on SMCs and reverse remodeling of pulmonary arteries. In the present study, phosphorylated ERK1/2 in the lung tissue was significantly increased after MCT injection. However, this increase was markedly attenuated by treatment with ONO-1301MS. ERK is the final component of the mitogen-activated protein kinase cascade. Prostacyclin has been shown to inhibit phosphorylation of ERK1/2 through the activation of cAMP (29). With respect to this signaling, protein kinase A (PKA), an intracellular effector of cAMP, has been shown to negatively regulate the Ras–ERK cascade by phosphorylating Raf and by preventing its association with active Ras (30). Furthermore, we previously reported that ONO-1301 inhibited pulmonary fibroblast proliferation through activation of the cAMP/PKA pathway (31). Therefore, it is interesting to speculate that ONO-1301MS may have antiproliferative effects on pulmonary vascular SMCs at least in part through inhibition of ERK via a cAMP-dependent pathway, although the precise mechanism remains to be elucidated.

ONO-1301MS significantly decreased urinary level of 11-$DTXB_2$, a metabolite of TXA_2. TXA_2 is a vasoconstrictor and a potent stimulator of platelet aggregation (32, 33). Moreover, it has been demonstrated that TXA_2 induces mitosis in vascular SMCs through activation of ERK (34, 35). It has been suggested that imbalance of thromboxane and prostacyclin plays an important role in the development of pulmonary hypertension (36). Previous reports showed that administration of thromboxane synthase inhibitor modestly attenuated pulmonary hypertension (37, 38). Thus, an inhibitory effect of ONO-1301MS on thromboxane synthase may also contribute to improvement in pulmonary hypertension.

In the present study, no adverse reactions, such as flushing, diarrhea, hypotension, renal dysfunction, or hepatic dysfunction, were observed in the treated group. However, further preclinical studies are necessary to confirm the safety and efficacy of ONO-1301MS before clinical trials start in patients with pulmonary arterial hypertension.

We did not measure cardiac output because of technical and mechanical problems. To support our hemodynamic data, we evaluated a variety of indexes, such as RV/BW and medial wall thickness of pulmonary arteries. These physiologic and histologic findings have been consistent with data on RV systolic pressure. Therefore, it is unlikely that the reduction in RV systolic pressure observed in the present study was related to the reduced cardiac output.

In conclusion, we developed a novel sustained-release prostacyclin analog polymerized with PLGA microspheres (ONO-1301MS), which achieved a 3-week elevation of its circulating level and simultaneously increased plasma cAMP levels for over 2 weeks, and had an inhibitory effect on thromboxane synthase. A single subcutaneous administration of ONO-1301MS attenuated MCT-induced pulmonary hypertension in rats. ONO-1301MS may have an antiproliferative effect through inhibition of ERK phosphorylation. This drug delivery system for a prostacyclin analog may be a new therapeutic strategy for the treatment of pulmonary arterial hypertension.

Conflict of Interest Statement: None of the authors has a financial relationship with a commercial entity that has an interest in the subject of this manuscript.

References

1. McLaughlin VV, McGoon MD. Pulmonary arterial hypertension. *Circulation* 2006;114:1417–1431.
2. Moncada S, Gryglewski R, Bunting S, Vane JR. An enzyme isolated from arteries transforms prostaglandin endoperoxides to an unstable substance that inhibits platelet aggregation. *Nature* 1976;263:663–665.
3. Moncada S, Vane JR. Arachidonic acid metabolites and the interactions between platelets and blood-vessel walls. *N Engl J Med* 1979;300: 1142–1147.
4. Humbert M, Sitbon O, Simonneau G. Treatment of pulmonary arterial hypertension. *N Engl J Med* 2004;351:1425–1436.
5. McLaughlin VV, Genthner DE, Panella MM, Rich S. Reduction in pulmonary vascular resistance with long-term epoprostenol (prostacyclin) therapy in primary pulmonary hypertension. *N Engl J Med* 1998;338:273–277.
6. McLaughlin VV, Shillington A, Rich S. Survival in primary pulmonary hypertension: the impact of epoprostenol therapy. *Circulation* 2002; 106:1477–1482.
7. Sitbon O, Humbert M, Nunes H, Parent F, Garcia G, Herve P, Rainisio M, Simonneau G. Long-term intravenous epoprostenol infusion in primary pulmonary hypertension: prognostic factors and survival. *J Am Coll Cardiol* 2002;40:780–788.
8. Okano Y, Yoshioka T, Shimouchi A, Satoh T, Kunieda T. Orally active prostacyclin analogue in primary pulmonary hypertension. *Lancet* 1997;349:1365.
9. Nagaya N, Uematsu M, Okano Y, Satoh T, Kyotani S, Sakamaki F, Nakanishi N, Miyatake K, Kunieda T. Effect of orally active prostacyclin analogue on survival of outpatients with primary pulmonary hypertension. *J Am Coll Cardiol* 1999;34:1188–1192.
10. Olschewski H, Simonneau G, Galie N, Higenbottam T, Naeije R, Rubin LJ, Nikkho S, Speich R, Hoeper MM, Behr J, *et al.* Inhaled iloprost for severe pulmonary hypertension. *N Engl J Med* 2002;347:322–329.
11. Simonneau G, Barst RJ, Galie N, Naeije R, Rich S, Bourge RC, Keogh A, Oudiz R, Frost A, Blackburn SD, *et al.* Continuous subcutaneous infusion of treprostinil, a prostacyclin analogue, in patients with pulmonary arterial hypertension: a double-blind, randomized, placebo-controlled trial. *Am J Respir Crit Care Med* 2002;165:800–804.
12. Badesch DB, McLaughlin VV, Delcroix M, Vizza CD, Olschewski H, Sitbon O, Barst RJ. Prostanoid therapy for pulmonary arterial hypertension. *J Am Coll Cardiol* 2004;43:56S–61S.
13. Laliberte K, Arneson C, Jeffs R, Hunt T, Wade M. Pharmacokinetics and steady-state bioequivalence of treprostinil sodium (Remodulin) administered by the intravenous and subcutaneous route to normal volunteers. *J Cardiovasc Pharmacol* 2004;44:209–214.
14. Kataoka M, Nagaya N, Satoh T, Itoh T, Murakami S, Iwase T, Miyahara Y, Kyotani S, Sakai Y, Kangawa K, *et al.* A long-acting prostacyclin agonist with thromboxane inhibitory activity for pulmonary hypertension. *Am J Respir Crit Care Med* 2005;172:1575–1580.
15. Alonso MJ, Gupta RK, Min C, Siber GR, Langer R. Biodegradable microspheres as controlled-release tetanus toxoid delivery systems. *Vaccine* 1994;12:299–306.
16. Seagal J, Edry E, Keren Z, Leider N, Benny O, Machluf M, Melamed D. A fail-safe mechanism for negative selection of isotype-switched B cell precursors is regulated by the Fas/FasL pathway. *J Exp Med* 2003;198:1609–1619.
17. Mullerad J, Cohen S, Benharroch D, Apte RN. Local delivery of IL-1 alpha polymeric microspheres for the immunotherapy of an experimental fibrosarcoma. *Cancer Invest* 2003;21:720–728.
18. Mullerad J, Cohen S, Voronov E, Apte RN. Macrophage activation for the production of immunostimulatory cytokines by delivering interleukin 1 via biodegradable microspheres. *Cytokine* 2000;12:1683–1690.
19. Sanchez A, Gupta RK, Alonso MJ, Siber GR, Langer R. Pulsed controlled-released system for potential use in vaccine delivery. *J Pharm Sci* 1996;85:547–552.
20. Roullin VG, Lemaire L, Venier-Julienne MC, Faisant N, Franconi F, Benoit JP. Release kinetics of 5-fluorouracil-loaded microspheres on an experimental rat glioma. *Anticancer Res* 2003;23:21–25.
21. Kimura H, Kasahara Y, Kurosu K, Sugito K, Takiguchi Y, Terai M, Mikata A, Natsume M, Mukaida N, Matsushima K, *et al.* Alleviation of monocrotaline-induced pulmonary hypertension by antibodies to monocyte chemotactic and activating factor/monocyte chemoattractant protein-1. *Lab Invest* 1998;78:571–581.
22. Ono S, Voelkel NF. PAF antagonists inhibit monocrotaline-induced lung injury and pulmonary hypertension. *J Appl Physiol* 1991;71:2483–2492.
23. Itoh T, Nagaya N, Fujii T, Iwase T, Nakanishi N, Hamada K, Kangawa K, Kimura H. A combination of oral sildenafil and beraprost ameliorates pulmonary hypertension in rats. *Am J Respir Crit Care Med* 2004;169:34–38.
24. Fiorucci S, Mencarelli A, Meneguzzi A, Lechi A, Morelli A, del Soldato P, Minuz P. NCX-4016 (NO-aspirin) inhibits lipopolysaccharide-induced tissue factor expression in vivo: role of nitric oxide. *Circulation* 2002;106:3120–3125.
25. Shive MS, Anderson JM. Biodegradation and biocompatibility of PLA and PLGA microspheres. *Adv Drug Deliv Rev* 1997;28:5–24.
26. Fornara P, Jocham D. Clinical study results of the new formulation leuprorelin acetate three-month depot for the treatment of advanced prostate carcinoma. *Urol Int* 1996;56:18–22.
27. Schmid P, Untch M, Kosse V, Bondar G, Vassiljev L, Tarutinov V, Lehmann U, Maubach L, Meurer J, Wallwiener D, *et al.* Leuprorelin acetate every-3-months depot versus cyclophosphamide, methotrexate, and fluorouracil as adjuvant treatment in premenopausal patients with node-positive breast cancer: the TABLE study. *J Clin Oncol* 2007;25:2509–2515.
28. Beghetti M, Reber G, de Moerloose P, Vadas L, Chiappe A, Spahr-Schopfer I, Rimensberger PC. Aerosolized iloprost induces a mild but sustained inhibition of platelet aggregation. *Eur Respir J* 2002; 19:518–524.
29. Li RC, Cindrova-Davies T, Skepper JN, Sellers LA. Prostacyclin induces apoptosis of vascular smooth muscle cells by a cAMP-mediated inhibition of extracellular signal-regulated kinase activity and can counteract the mitogenic activity of endothelin-1 or basic fibroblast growth factor. *Circ Res* 2004;94:759–767.
30. Cook SJ, McCormick F. Inhibition by cAMP of Ras-dependent activation of Raf. *Science* 1993;262:1069–1072.
31. Murakami S, Nagaya N, Itoh T, Kataoka M, Iwase T, Horio T, Miyahara Y, Sakai Y, Kangawa K, Kimura H. Prostacyclin agonist with thromboxane synthase inhibitory activity (ONO-1301) attenuates bleomycin-induced pulmonary fibrosis in mice. *Am J Physiol Lung Cell Mol Physiol* 2006;290:L59–L65.
32. Hamberg M, Svensson J, Samuelsson B. Prostaglandin endoperoxides: a new concept concerning the mode of action and release of prostaglandins. *Proc Natl Acad Sci USA* 1974;71:3824–3828.
33. Svenssen J, Strandberg K, Tuvemo T, Hamberg M. Thromboxane A2: effects on airway and vascular smooth muscle. *Prostaglandins* 1977; 14:425–436.
34. Sachinidis A, Flesch M, Ko Y, Schror K, Bohm M, Dusing R, Vetter H. Thromboxane A2 and vascular smooth muscle cell proliferation. *Hypertension* 1995;26:771–780.
35. Morinelli TA, Tempel GE, Jaffa AA, Silva RH, Naka M, Folger W, Halushka PV. Thromboxane A2/prostaglandin H2 receptors in streptozotocin-induced diabetes: effects of insulin therapy in the rat. *Prostaglandins* 1993;45:427–438.
36. Christman BW, McPherson CD, Newman JH, King GA, Bernard GR, Groves BM, Loyd JE. An imbalance between the excretion of thromboxane and prostacyclin metabolites in pulmonary hypertension. *N Engl J Med* 1992;327:70–75.
37. Nagata T, Uehara Y, Hara K, Igarashi K, Hazama H, Hisada T, Kimura K, Goto A, Omata M. Thromboxane inhibition and monocrotaline-induced pulmonary hypertension in rats. *Respirology* 1997;2:283–289.
38. Rich S, Hart K, Kieras K, Brundage BH. Thromboxane synthetase inhibition in primary pulmonary hypertension. *Chest* 1987;91:356–360.

Am J Physiol Heart Circ Physiol 294: H441–H448, 2008.
First published November 16, 2007; doi:10.1152/ajpheart.01021.2007.

Role of Cu,Zn-SOD in the synthesis of endogenous vasodilator hydrogen peroxide during reactive hyperemia in mouse mesenteric microcirculation in vivo

Toyotaka Yada,[1] Hiroaki Shimokawa,[2] Keiko Morikawa,[3] Aya Takaki,[2] Yoshiro Shinozaki,[4] Hidezo Mori,[5] Masami Goto,[1] Yasuo Ogasawara,[1] and Fumihiko Kajiya[1]

[1]*Department of Medical Engineering and Systems Cardiology, Kawasaki Medical School, Kurashiki, Japan;* [2]*Department of Cardiovascular Medicine, Tohoku University Graduate School of Medicine, Sendai, Japan;* [3]*Department of Anesthesiology, Kyushu University Graduate School of Medical Sciences, Fukuoka, Japan;* [4]*Department of Physiology, Tokai University School of Medicine, Isehara, Japan; and* [5]*Department of Cardiac Physiology, National Cardiovascular Center Research Institute, Suita, Japan*

Submitted 4 September 2007; accepted in final form 12 November 2007

Yada T, Shimokawa H, Morikawa K, Takaki A, Shinozaki Y, Mori H, Goto M, Ogasawara Y, Kajiya F. Role of Cu,Zn-SOD in the synthesis of endogenous vasodilator hydrogen peroxide during reactive hyperemia in mouse mesenteric microcirculation in vivo. *Am J Physiol Heart Circ Physiol* 294: H441–H448, 2008. First published November 16, 2007; doi:10.1152/ajpheart.01021.2007.—We have recently demonstrated that endothelium-derived hydrogen peroxide (H_2O_2) is an endothelium-derived hyperpolarizing factor and that endothelial Cu/Zn-superoxide dismutase (SOD) plays an important role in the synthesis of endogenous H_2O_2 in both animals and humans. We examined whether SOD plays a role in the synthesis of endogenous H_2O_2 during in vivo reactive hyperemia (RH), an important regulatory mechanism. Mesenteric arterioles from wild-type and Cu,Zn-SOD$^{-/-}$ mice were continuously observed by a pencil-type charge-coupled device (CCD) intravital microscope during RH (reperfusion after 20 and 60 s of mesenteric artery occlusion) in the cyclooxygenase blockade under the following four conditions: control, catalase alone, N^G-monomethyl-L-arginine (L-NMMA) alone, and L-NMMA + catalase. Vasodilatation during RH was significantly decreased by catalase or L-NMMA alone and was almost completely inhibited by L-NMMA + catalase in wild-type mice, whereas it was inhibited by L-NMMA and L-NMMA + catalase in the Cu,Zn-SOD$^{-/-}$ mice. RH-induced increase in blood flow after L-NMMA was significantly increased in the wild-type mice, whereas it was significantly reduced in the Cu,Zn-SOD$^{-/-}$ mice. In mesenteric arterioles of the Cu,Zn-SOD$^{-/-}$ mice, Tempol, an SOD mimetic, significantly increased the ACh-induced vasodilatation, and the enhancing effect of Tempol was decreased by catalase. Vascular H_2O_2 production by fluorescent microscopy in mesenteric arterioles after RH was significantly increased in response to ACh in wild-type mice but markedly impaired in Cu,Zn-SOD$^{-/-}$ mice. Endothelial Cu,Zn-SOD plays an important role in the synthesis of endogenous H_2O_2 that contributes to RH in mouse mesenteric smaller arterioles.

nitric oxide; endothelium-derived hyperpolarizing factor; arteriole; vasodilatation

THE ENDOTHELIUM SYNTHESIZES and releases endothelium-derived relaxing factors (EDRFs), including vasodilator prostaglandins, nitric oxide (NO), and as yet unidentified endothelium-derived hyperpolarizing factor (EDHF). Since the first reports on the existence of EDHFs (4, 8), several candidates for EDHF have been proposed (9), including cytochrome *P*-450 metabolites (2, 3), endothelium-derived K^+ channel (7), and electrical communications through gap junctions between endothelial cells and vascular smooth muscle cells (34). Matoba et al. (19a, 19b, 20) previously identified that endothelium-derived hydrogen peroxide (H_2O_2) is a primary EDHF in mesenteric arteries of mice, pigs, and humans. Morikawa et al. (24a, 25) subsequently confirmed that endothelial Cu/Zn-superoxide dismutase (SOD) plays an important role in synthesizing EDHF/H_2O_2 in mice and humans. Recently, our laboratory (41a, 42) confirmed that endogenous H_2O_2 plays an important role for autoregulation and protection against reperfusion injury in canine coronary microcirculation.

Reactive hyperemia (RH) is an important regulatory mechanism of the cardiovascular system in response to a temporal reduction in blood flow for which both mechanosensitive (e.g., myogenic and shear mediated) and metabolic regulatory processes may be involved (6, 14a, 28). For the RH response of canine coronary microcirculation, NO, ATP-sensitive K^+ channels, and adenosine may all be involved (11, 41). Shear stress plays a crucial role in modulating vascular tone by stimulating the release of EDRFs (8, 32), and all three EDRFs (PGI_2, NO, and EDHF) are involved in flow-induced vasodilatation (15, 18, 33, 44).

However, it remains to be examined whether endogenous H_2O_2 is involved in the vasodilator mechanism of RH and, if so, whether endothelial Cu,Zn-SOD plays a role in the synthesis of endogenous H_2O_2 during RH. The present study was thus designed to address these important issues in mice. Our laboratory (42, 44) previously reported that the contribution of EDHF to the vasodilatory mechanisms increases as the diameter of the vessel decreases. Thus, by employing a pencil-type charge-coupled device (CCD) intravital microscope with a high resolution, we focused on the arterioles with a diameter of <50 μm in vivo.

METHODS

The present study was approved by the Animal Care and Use Committee of Kawasaki Medical School and conformed to the guidelines on animal experiments of Kawasaki Medical School and *the*

Address for reprint requests and other correspondence: Toyotaka Yada, Dept. of Medical Engineering and Systems Cardiology, Kawasaki Medical School, 577 Matsushima, Kurashiki, Okayama 701-0192 Japan (e-mail: yada@me.kawasaki-m.ac.jp).

The costs of publication of this article were defrayed in part by the payment of page charges. The article must therefore be hereby marked "*advertisement*" in accordance with 18 U.S.C. Section 1734 solely to indicate this fact.

Guide for the Care and Use of Laboratory Animals published by the National Institutes of Health.

Animal preparation. Male Cu,Zn-SOD$^{-/-}$ and control mice (10–16 wk of age) derived from breeding pairs of heterozygous (Cu,Zn-SOD$^{+/-}$) mice (Jackson Laboratory, Bar Harbor, ME) were used (25). They were placed on a heating blanket to maintain body temperature at 37°C throughout the experiment. The animals were anesthetized with 1% inhalational anesthesia of isoflurane. After tracheal intubation, they were ventilated with a mixture of room air and oxygen by a ventilator. The abdomen was opened, and a 24-Fr catheter was inserted into the abdominal aorta to measure aortic pressure. Mesenteric arterioles were continuously observed by a pencil-type intravital microscope (Nihon Kohden, Tokyo, Japan) (13).

Measurements of diameter by pencil-type intravital microscope. Mesenteric arterioles were visualized using a pencil-type intravital microscope (13). The system was modified for the visualization of microcirculation from our previous needle-probe CCD videomicroscope system (40). The microscopic images were monitored and recorded on a digital videocassette recorder (Sony, Tokyo, Japan) every 33 ms (30 frames/s). The spatial resolution of a static image of this system is 0.5 μm for ×600 magnification. The field of view is 367 × 248 μm, and the focal depth is 50 μm.

Measurements of regional blood flow in mesenteric arteries. Regional blood flow in mesenteric arteries was measured by the nonradioactive microsphere (15 μm; Sekisui Plastic, Tokyo, Japan) technique at the end of the experiments, as previously described (24). Briefly, a bolus (50 μl) of the microspheres suspension (5×10^5 spheres; Ce and Ba) were injected into the abdominal aorta at baseline and 5 s after the reperfusion of the mesenteric artery with confirming changes of the blood flow of the mesenteric artery by a CCD intravital microscope and without inducing hemodynamic changes (14). Mice were euthanized, and the mesenterium was extracted. The X-ray fluorescence of the stable heavy elements was measured by a wavelength-dispersive spectrometer (model PW 1480; Phillips, Eindhoven, the Netherlands). The relative increase in blood flow of mesenterium [microsphere count/tissue weight (g)] during RH from baseline was calculated.

Detection of H_2O_2 and NO production in mesenteric microvessels. 2′,7′-Dichlorodihydrofluorescein diacetate (DCF-DA; Molecular Probes, Eugene, OR) and diaminorhodamine-4M AM (DAR; Daiichi Pure Chemicals, Tokyo, Japan) were used to detect H_2O_2 and NO production in mesenteric microvessels, respectively, as previously described (41a). Briefly, fresh and unfixed mesenteric tissue was cut into several blocks and immediately frozen in an optimal cutting temperature compound (Tissue-Tek; Sakura Fine Chemical, Tokyo, Japan). After washout of the mesenteric tissue with phosphate-buffered solution under a normal temperature, fluorescent images of the microvessels were obtained 3 min after application of acetylcholine (ACh) by using a fluorescence microscope (Olympus BX51) (41a). We defined the baseline fluorescent intensity as the response in the vascular endothelium just after the injection of NO or H_2O_2 fluorescent dye. The fluorescence data at baseline (both DCF-DA and DAR) were obtained after the RH.

Experimental protocol. We performed four protocols. First, mesenteric arterioles in wild-type and Cu,Zn-SOD$^{-/-}$ mice were continuously observed by a pencil-type intravital microscope during RH (reperfusion after 20 and 60 s of mesenteric artery occlusion) with cyclooxygenase blockade [indomethacin, 5×10^{-5} mol/l topical administration (ta)] with the following four conditions: control, catalase alone [1,500 U·min^{-1}·100 g body wt^{-1} intra-arterial administration (ia) polyethylene glycol-catalase, a specific decomposer of H_2O_2], NO synthase inhibitor alone (10^{-4} mol/l ta L-NMMA), and L-NMMA + catalase (17). In the presence of indomethacin and L-NMMA, microspheres were administered at baseline and 5 s after the reperfusion into the abdominal aorta by bolus injection because RH peaked within 20–60 s after release from 20- and 60-s occlusion (29). Maximal vascular diameter was measured within 20 and 60 s after the reperfusion. Second, ACh (10^{-7} to 10^{-5} mol/l ta)-induced endothelium-dependent vasodilatation was examined under the control conditions and in the presence of Tempol, a SOD mimetic 4-hydroxy-2,2,6,6-tetramethylpiperidine-*N*-oxyl (50 μg·min^{-1}·100 g body wt^{-1} ia) (17), and Tempol + catalase. In the combined infusion protocol (Tempol or Tempol + catalase) in the presence of cyclooxygenase blockade + L-NMMA, the combined infusion was performed simultaneously for 20 min, ACh was infused for 10 min, and the vascular diameter was measured. Third, sodium nitroprusside (SNP; 10^{-7} to 10^{-5} mol/l ta, each 10 min)-induced endothelium-independent vasodilatation was examined in wild-type and Cu,Zn-SOD$^{-/-}$ mice. Fourth, fresh and unfixed mesenteric tissue was then cut into several blocks and immediately frozen in optimal cutting temperature compound.

Statistical analysis. The results are expressed as means ± SE. Dose-response curves were analyzed by two-way ANOVA followed by the Scheffé's post hoc test for multiple comparisons. Vascular responses were analyzed by one-way ANOVA followed by the Scheffé's post hoc test for multiple comparisons. $P < 0.05$ was considered to be statistically significant.

RESULTS

Hemodynamics and blood gases during RH. Throughout the experiments, mean aortic pressure and heart rate were constant and comparable (Tables 1 and 2), and Po_2, Pco_2, and pH were maintained within the physiological ranges (>70 mmHg Po_2, 25–40 mmHg Pco_2, and pH 7.35–7.45). Baseline mesenteric

Table 1. *Hemodynamics during RH*

		Control		Catalase		L-NMMA		L-NMMA + Catalase	
	n	B	RH	B	RH	B	RH	B	RH
MBP, RH 20, mmHg									
WT	10	83±7	85±9	81±7	82±7	82±8	81±6	83±8	82±6
Cu/Zn-SOD$^{-/-}$	10	85±12	87±10	83±8	82±8	82±8	82±8	82±8	80±9
MBP, RH 60, mmHg									
WT	5	86±8	88±7	87±7	88±7	88±8	87±7	88±7	87±7
Cu/Zn-SOD$^{-/-}$	5	88±8	86±8	87±6	89±9	88±7	88±8	89±6	90±11
HR, RH 20, beats/min									
WT	10	346±14	348±14	335±15	333±17	315±15	310±17	330±18	330±18
Cu/Zn-SOD$^{-/-}$	10	364±27	354±22	350±18	351±15	355±15	340±17	355±15	335±17
HR, RH 60, beats/min									
WT	5	351±31	361±9	353±21	356±13	358±10	364±37	354±22	355±15
Cu/Zn-SOD$^{-/-}$	5	346±18	356±25	356±15	361±19	351±31	361±9	358±10	364±27

Values are means ± SE; *n*, number of rats. RH, reactive hyperemia; L-NMMA, N^G-monomethyl-L-arginine; B, baseline; MBP, mean blood pressure; HR, heart rate; WT, wild-type.

Table 2. *Hemodynamics during administration of ACh and SNP*

		Control			Tempol			Tempol + Catalase			SNP		
	n	B	ACh 10^{-7}	ACh 10^{-6}	ACh 10^{-5}	ACh 10^{-7}	ACh 10^{-6}	ACh 10^{-5}	ACh 10^{-7}	ACh 10^{-6}	ACh 10^{-5}	B	SNP 10^{-7}	SNP 10^{-6}	SNP 10^{-5}
MBP, mmHg															
WT	10	90±7	88±7	87±7	89±6	91±10	90±11	84±11	91±8	86±8	86±8	78±13	77±13	76±13	76±13
Cu/Zn-SOD$^{-/-}$	10	93±11	92±10	94±10	97±10	98±16	97±15	99±15	91±8	91±8	88±8	81±8	77±10	75±11	74±11
HR, beats/min															
WT	10	361±9	340±17	340±17	340±17	342±24	336±25	336±25	320±19	330±27	330±27	370±57	364±37	351±31	351±31
Cu/Zn-SOD$^{-/-}$	10	386±11	381±24	371±21	396±13	386±11	377±15	377±15	362±22	356±25	356±25	372±21	369±6	358±10	346±18

Values are means ± SE; *n*, number of rats. SNP, sodium nitroprusside; ACh, acetylcholine.

arteriolar diameter was comparable in the absence and presence of inhibitors under the four different experimental conditions (Tables 3 and 4). Those different inhibitors (L-NMMA, catalase, and Tempol) did not affect basal diameter.

Mesenteric vasodilatation during RH. We were able to observe EDHF-sensitive smaller arterioles (18–66 μm) by using a newly developed pencil-type CCD intravital microscope with a higher resolution. In the mesenteric arterioles of wild-type mice, vasodilatation during RH to 20- and 60-s arterial occlusion was decreased by catalase or L-NMMA alone and was almost completely inhibited by L-NMMA + catalase (Fig. 1). In contrast, in mesenteric arterioles of Cu,Zn-SOD$^{-/-}$ mice, vasodilatation during RH to 20- and 60-s arterial occlusion was decreased by catalase alone and was almost completely inhibited by L-NMMA alone or L-NMMA + catalase (Fig. 1). Blood flow measurement by microsphere technique showed that in the presence of indomethacin and L-NMMA, RH-induced increase in blood flow was 232 ± 4% (20 s) and 331 ± 4% (60 s) of baseline in control and was sensitive to catalase (137 ± 4%, 20 s; and 147 ± 17%, 60 s) in the wild-type mice, whereas in the Cu,Zn-SOD$^{-/-}$ mice, the vasodilator response was significantly reduced to 125 ± 19% (20 s) and 145 ± 23% (60 s) in control and was insensitive to catalase (120 ± 24%, 20 s; and 139 ± 19%, 60 s) (Fig. 2). With the longer occlusion of the mesenteric artery, the shear stimulus for H_2O_2 release was significantly increased in the control condition and was significantly decreased by catalase.

Endothelium-dependent vasodilatation. In mesenteric arterioles of wild-type mice, endothelium-dependent vasodilatation to ACh (10^{-7} to 10^{-5} mol/l in the presence of indomethacin and L-NMMA) was unchanged with Tempol but significantly inhibited by the addition of catalase (Fig. 3). In contrast, in the mesenteric arterioles of the Cu,Zn-SOD$^{-/-}$ mice, the response to ACh was significantly enhanced with Tempol, a response that was sensitive to the addition of catalase (Fig. 3).

Endothelium-independent vasodilatation. Endothelium-independent vasodilatation to SNP (10^{-7} to 10^{-5} mol/l in the presence of L-NMMA + catalase) was comparable between the two strains (Table 4).

Detection of H_2O_2 and NO production in the mesenteric artery. Fluorescent microscopy with DCF-DA showed that vascular H_2O_2 production in mesenteric arterioles was significantly increased in response to ACh in wild-type mice compared with baseline but markedly impaired in Cu,Zn-SOD$^{-/-}$ mice (Fig. 4). In contrast, vascular NO production in mesenteric arterioles, as assessed by DAR fluorescent intensity, was significantly increased in response to ACh in wild-type mice compared with baseline and was unaltered in Cu,Zn-SOD$^{-/-}$ mice (Fig. 5).

DISCUSSION

The novel finding of the present study with a newly developed pencil-type CCD intravital microscope in vivo is that Cu,Zn-SOD plays an important role in the synthesis of endogenous H_2O_2, which is substantially involved in the mechanisms of RH-induced vasodilatation in mouse mesenteric circulation.

Impaired EDHF-mediated vasodilatation in Cu,Zn-SOD$^{-/-}$ mice in vivo. Matoba et al. (19a, 20) have previously identified that endothelium-derived H_2O_2 is an EDHF in mouse and